Politecnico di Torino

Politecnico di Torino

Master's Degree in Aerospace Engineering

Academic Year 2024/2025

Graduation Session December 2025

CFD Modeling and Simulation of Combustion in a Hybrid Rocket Engine

Supervisors:

Prof. Dario G. Pastrone
Prof. Andrea Ferrero
Ph.D. Lorenzo Folcarelli
Prof. Filippo Masseni

Candidate:

Michele Giampalmo

Abstract

In recent years, hybrid rocket engines have played an increasingly important role in space propulsion, thanks to their operational safety and unique functional characteristics. Their restart capability, thrust modulation, structural simplicity, low cost, and flexibility in propellant selection are particularly noteworthy.

This makes them suitable for a wide range of applications, such as primary propulsion for launchers, upper stage propulsion and space transportation. In addition, the growing focus on reducing development costs, environmental sustainability, and propulsion system reliability has increased interest in this type of engine.

However, they have some limitations, in particular low regression rates and mixing problems, which can lead to incomplete combustion, reduce engine efficiency, and make accurate performance prediction difficult.

To address these issues, numerical modeling and CFD simulations are essential tools, capable of describing combustion and grain regression phenomena in greater detail than empirical models alone.

In this context, this work focuses on the study conducted by Prof. M. Arif Karabeyoglu on a hybrid rocket engine using high-density polyethylene (HDPE) as fuel and gaseous oxygen as oxidizer. The objective is to analyze the fluid-dynamic and chemical behavior inside the combustion chamber and to evaluate the engine's performance through a numerical approach.

Table of Contents

List of Tables

List of Figures

Glossary

HRE
: Hybrid Rocket Engine

JPL
: Jet Propulsion Laboratory

LRE
: Liquid Rocket Engine

SRE
: Solid Rocket Engine

LOX
: Liquid Oxygen

GE
: General Electric Company

PMM
: Polymethylmethacrylate

UTC
: United Technologies Center

MON-25
: Mixed Oxides of Nitrogen

IRFNA
: Inhibited Red Fuming Nitric Acid

PB

Polybutadiene

HTPB

Hydroxyl-Terminated Polybutadiene

AMROC

American Rocket Company

eAc

Environmental Aeroscience Corporation

USAF

United States Air Force

SPG

Space Propulsion Group

NASA

National Aeronautics and Space Administration

DLR

Deutsches Zentrum für Luft- und Raumfahrt

HYDRA

HYbrid Demonstration Rocket for Applications

HYFIRE

HYbrid FIRE test program

FLOX

Fluorine–Oxygen Mixture

HAST

Hybrid Advanced Suborbital Test

JP

Jet Propellant

ONERA

Office National d'Études et de Recherches Aérospatiales

Nucleus

Programma sperimentale ibrido di Nammo (Norvegia)

SL1

Small Launcher 1

HDPE

High Density Polyethylene

CEA

Chemistry Equilibrium with Applications

DNS

Direct Numerical Simulation

LES

Large Eddy Simulation

RANS

Reynolds-Averaged Navier-StokeS

DES

Detatched Eddy Simulation

DDES

Delayed Detatched Eddy Simulation

UCSD

University of California at San Diego

SST

Shear Stress Transport

LPT

Low Pressure Turbine

HPT

High Pressure Turbine

EDM

Eddy Dissipation Model

PDF

Probability Density Function

FGM

Flamelet Generated Mainfold

TCI

Turbulence–Chemistry Interaction

EDC

Eddy Dissipation Concept

FSM

Fractional Step Method

FVM

Finite Volume Method

FOU

First Order Upwind

SOU

Second Order Upwind

ODE

Ordinary Differential Equation

CFL

Courant-Friedrichs-Lewy

Chapter 1

Introduction

Propulsion, understood as the generation of thrust, is based on the principle of action and reaction. In general, propulsion systems can be divided into two broad categories:

- *Reciprocating engines*, in which thrust is obtained by converting the mechanical power produced by a crankshaft, as in the case of piston engines coupled to propellers.
- *Jet propulsion*, which generates thrust by expelling mass at high speed, thus producing a reaction force. This category includes turbofan, turbojet, and rocket engines.

Jet propulsion can be further classified into:

- *Duct propulsion*, which uses atmospheric air as an oxidizer (e.g., turbojets, turbofans, ramjets, and scramjets).
- *Rocket propulsion*, which uses propellants stored on board, making the system independent of the external environment.

1.1 Types of Rocket Propulsion

The energy sources used to generate thrust can be of different types. Propulsion can be based on chemical reactions, obtained by combining a fuel with an oxidizer, on the use of solar radiation, or on nuclear processes.

Based on their operating principle, propulsion systems can be classified into three macro-categories, described in the following paragraphs.

1.1.1 Nuclear Propulsion

Nuclear propulsion uses energy in two ways:

- A nuclear generator produces electricity, which is then used in an electric propulsion system.
- Fission reactors are used to heat a gas, causing it to expand in a nozzle and generate thrust.

These systems are generally lightweight and capable of taking off autonomously, as they can generate thrust equal to 3–4 times their own weight. However, their performance is limited by the maximum temperature of the gases that the engine structure can withstand. Furthermore, the exhaust gases are radioactive, making it impossible to use such engines during the ascent phase in the Earth's atmosphere.

1.1.2 Electric Propulsion

Electric propulsion uses electrical energy to accelerate a propellant, achieving high exhaust velocities with relatively low thrust. The main modes of operation can be divided into three categories:

- heating the gas using an electrical resistance, then expanding it through the nozzle (electrothermal propulsion);
- accelerating particles using electric fields (electrostatic propulsion);
- exploiting forces generated by the interaction between electric and magnetic fields (electromagnetic propulsion).

The main strength of this technology is its high versatility: with the same available electrical power P_e, a reduction in thrust T or propellant mass flow rate $\dot{m}_p$ allows higher specific impulse values to be obtained .

On the other hand, the unfavorable ratio between power required and thrust generated prevents these systems from producing sufficient acceleration for takeoff from Earth.

1.1.3 Chemical Propulsion

In chemical propulsion, there are three main types of rockets:

- *Liquid rocket engines*, which can be single-propellant, dual-propellant, or, more rarely, triple-propellant. In these systems, the propellants are stored in liquid form and mixed in the combustion chamber.

- *Solid rocket motors*, in which the propellant is stored and consumed in solid form.

- *Hybrid rocket engines*, in which the fuel is generally in solid form and the oxidizer in liquid or gaseous form.

Liquid Rocket Engines

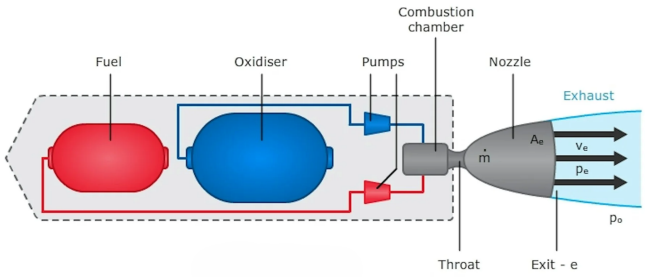

Figure 1.1: Schematic diagram of a liquid rocket engine [1]

These rockets use propellants stored in liquid form and introduced into the combustion chamber at high pressures. This requires a feeding and pressurization system, typically consisting of high-performance pumps or pressurized tanks.

The propellant is injected into the chamber through special injectors, where it is mixed and ignited according to a specific oxidizer-fuel ratio. The hot gases produced by combustion are then expanded in a convergent-divergent supersonic nozzle, generating propulsive thrust.

One of the main features of this category of engines is the possibility of being shut down and restarted several times, thanks to direct control over the injection of propellants. However, the fuel system represents a significant portion of the overall mass and introduces complex mechanical elements, resulting in increased weight and reduced overall engine reliability.

Solid Rocket Motors

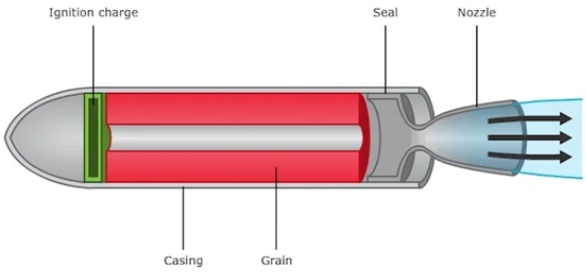

Figure 1.2: Diagram of a solid rocket [1]

The term "motor" indicates that this propulsor cannot be throttled or adjusted once ignited: combustion proceeds autonomously until the propellant is exhausted, making it impossible to modulate the thrust or shut down the motor during operation.

In this type of rocket, both the fuel and the oxidizer are stored inside the solid grain; consequently, no external fuel supply or pressurization system is required.

The main operational risk is deflagration-to-detonation transition (DDT), i.e., the undesirable transition from subsonic combustion to a detonation wave, capable of generating pressures that are destructive to the structure. A further danger is the accidental ignition of the propellant, which can be triggered by impact, high temperatures, or electrostatic stresses.

Hybrid Rocket Engines

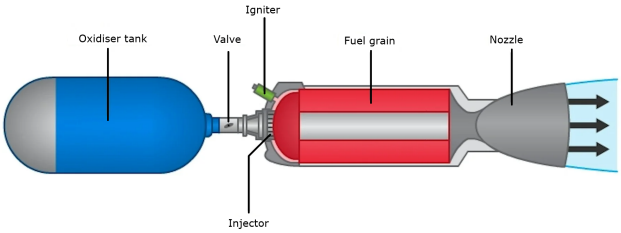

Figure 1.3: Diagram of a hybrid rocket [1]

Hybrids generally use oxidizers in liquid or gaseous phase and fuel in solid phase. The performance of this rocket is intermediate between the generally high performance of liquids and that of solids. Compared to liquid propulsion, it is less expensive and more reliable.

1.2 Definition of Hybrid Engine Performance

The performance of a rocket can be evaluated using analytical approaches, numerical models, or experimental tests. This performance can be classified into several categories:

- **real**, obtained from tests under operating conditions;
- **theoretical**, derived from ideal models or simplified assumptions;
- **under standard conditions**, referring to conventional parameters established for comparison between different configurations;
- **minimum guaranteed**, defined as design requirements that the system must meet.

Regardless of the type, performance parameters must be consistent with mission requirements and the expected flight profile.

It is also important to distinguish performance from its model representation: performance is a defined physical quantity, while its estimation in a theoretical context requires the adoption of a model that approximates its actual behavior.

Figure 1.4 shows a diagram of the thrust chamber.

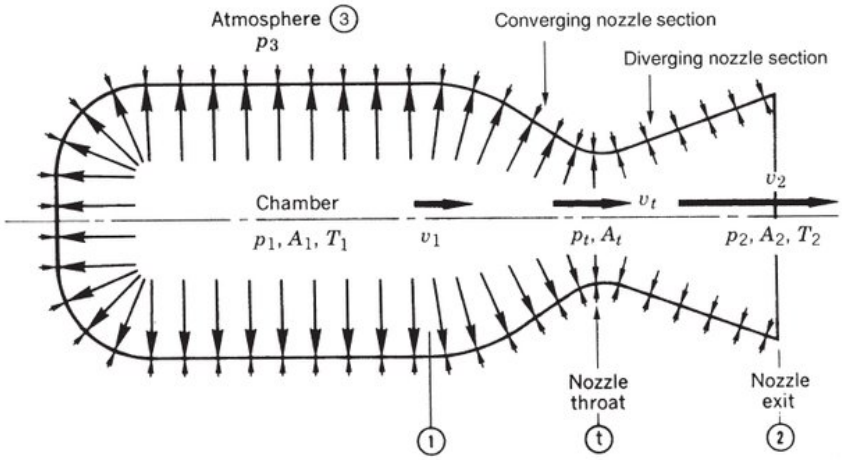

Figure 1.4: Thrust chamber

One of the fundamental parameters is *thrust*, defined as:

$$F = \dot{m} w_e + A_e(p_e - p_0)$$

where $\dot{m}$ is the total mass flow rate at the outlet, w_e is the outflow velocity, A_e is the outlet cross-sectional area, p_e is the static outlet pressure, and p_0 is the ambient pressure.

Thrust generally varies over time due to fuel regression and changes in oxidizer flow rate; for this reason, *total impulse* is introduced, which measures its overall intensity over time:

$$I_t = \int_0^{t_b} F(t)\, dt$$

where t_b represents the combustion time.

Another widely used parameter is the *specific impulse*, which represents the propulsive efficiency of the system. It is defined as:

$$I_{sp} = \frac{F}{\dot{m}\, g_0} = \frac{c}{g_0}$$

where g_0 is the acceleration due to gravity at sea level and c is the *effective exhaust velocity*:

$$c = \frac{F}{\dot{m}}$$

The latter represents the equivalent velocity that the exhaust gases should have, under adapted nozzle conditions, to generate the measured thrust.

The average specific impulse can be derived from the total impulse:

$$I_{sp,\,avg} = \frac{I_t}{g_0\, m_p}$$

where m_p is the total mass of propellant consumed during combustion.

An equally important parameter is the *characteristic velocity*:

$$c^* = \frac{p_c\, A_t}{\dot{m}} \tag{1.1}$$

where p_c is the average pressure in the combustion chamber and A_t is the throat area. It represents the thermochemical efficiency of the combustion process and allows propellants or combustion models to be compared independently of the nozzle geometry. High values of c^* indicate more complete combustion and better utilization of the available chemical energy.

The mixture ratio is an equally crucial design parameter, defined as:

$$r_m = \frac{\dot{m}_{ox}}{\dot{m}_f}$$

where $\dot{m}_{ox}$ and $\dot{m}_f$ are the oxidizer and fuel flow rates, respectively. This ratio affects the flame temperature, the composition of the products, and the overall efficiency of the engine.

Another important parameter is the thrust coefficient:

$$C_F = \frac{F}{p_c\, A_t}$$

which takes into account the expansion of gases in the nozzle and is closely related to the expansion ratio and the pressure ratio p_e/p_c.

Finally, the *combustion efficiency* can be expressed as:

$$\eta_c = \frac{c^*_{exp}}{c^*_{theor}}$$

where c^*_{theor} is the theoretical characteristic velocity obtained from thermochemical analyses (e.g., with NASA CEA) and c^*_{exp} is the experimental or numerical velocity.

This parameter measures how close the actual process is to the ideal conditions of complete combustion.

1.3 Ideal Rocket Model

The performance definitions can be used within an ideal rocket model. With appropriate assumptions, it is possible to apply the principles of thermodynamics in a simplified form. The classic assumptions are:

- **homogeneous flow** in the combustion chamber, with uniform properties in each section;
- **chemical equilibrium** in the combustion products;
- **perfect gas** with specific heat ratio $\gamma = \text{const}$;
- **adiabatic and isentropic expansion** in the nozzle, without heat exchange and without dissipation;
- **absence of shock waves or discontinuities** along the port and in the nozzle;
- **absence of boundary layer effects** on the walls;
- **one-dimensional flow** inside the nozzle;
- **predominantly axial velocity**, neglecting radial and tangential components;
- **steady state**, with constant mass flow rate over time.

Chapter 2

Historical perspective of hybrid propulsion

2.1 Introduction

Before going into detail, it is worth introducing the concept of the Hybrid Rocket Engine (HRE).

A rocket engine is a propulsion system in which combustion occurs within a closed chamber. The hot gases generated at high pressure are expanded through a nozzle, producing thrust according to the principle of action and reaction.

Unlike liquid-propellant rocket engines, which employ both fuel and oxidizer in liquid form, or solid-propellant rocket engines, where the propellants are pre-mixed in a single grain, hybrid rocket engines use propellants in different physical states.

In the most common configuration, the fuel is solid while the oxidizer is in a fluid phase (either liquid or gaseous), thus combining some of the main advantages of both liquid and solid propulsion systems.

2.2 History

This chapter provides an overview of the historical development of hybrid rocket engines, largely based on the discussion in Fundamentals of Hybrid Rocket Combustion and Propulsion by Chiaverini and Kuo [2].

2.2.1 Origins (1930s–1960s)

The first developments in Hybrid Rocket Engine date back to the 1930s, in parallel with the initial advances in liquid-propellant (LRE) and solid-propellant (SRE) rocket engines. The latter were the first to be used, thanks in part to the long

tradition associated with the use of gunpowder. However, they were soon abandoned due to their dangerous nature: in 1933, for example, Reinhold Tiling, one of the pioneers of rocketry, died along with three assistants following the explosion of approximately 40 pounds of gunpowder during an experimental test.

During those same years, Robert Goddard, another key figure in the development of propulsion, managed to reduce the risk of explosion by injecting small amounts of gunpowder into a separate combustion chamber, in order to control the combustion speed and prevent the entire fuel from being exposed to heat simultaneously. This approach also allowed for control of the engine's ignition and shutdown.

However, the inherent complexity of this system prompted Goddard to gradually focus on liquid propulsion: in 1935, he succeeded in achieving a successful flight, bringing a liquid-propellant rocket to an altitude of about 1.9 km.

The first documented attempt, considered a precursor to the hybrid rocket, is attributed to Sergei P. and Mikhail K. Tikhonravov. The launch of GRID-09 on August 17, 1933, involved a vehicle with a diameter of about 18 cm and a length of 2.4 m; the engine delivered approximately 500 N for 15 s, allowing it to reach an altitude of 1,500 m. Gelatinized gasoline (gasoline/rosin) suspended on a metal mesh and pressurized liquid oxygen (LOX) were used as propellants.

In the following years, starting in 1937, other studies on hybrid engines emerged: among these, at I.G. Farben, Leonid Andrussow, O. Lutz, and W. Noeggerath tested a 10 kN hybrid engine powered by coal and nitrous oxide. The tests did not produce the expected results due to the sublimation of coal, a phenomenon that reduced the combustion rate.

A first significant attempt was made in the mid-1940s by the Pacific Rocket Society. On that occasion, hybrid propulsion systems powered by liquid oxygen (LOX) as an oxidizer and various solid fuels, including Douglas fir wood, wax with carbon black additives, and rubber-based formulations, were tested.

Tests with fir wood-based propellants began in 1947. The initial configuration (XDF-3) featured a Douglas fir nozzle impregnated with a solution of zinc and ammonium chloride to improve its heat resistance. However, this solution proved ineffective: low-pressure combustion destroyed the nozzle in about 15 seconds. The next experiment (XDF-4) introduced an internal calcium sulfate coating, but the engine failed just two seconds after ignition due to excessive thrust. It took another 19 attempts to achieve a successful flight: in 1953, the XDF-23 rocket, equipped with LOX and a rubber-based fuel and fitted with an aluminum alloy nozzle, reached an altitude of just over 9 km.

Although no ballistic analysis was reported, a fundamental concept of hybrid combustion was outlined during this period: the pressure in the combustion chamber does not depend directly on the internal surface of the fuel exposed to the flame, but is proportional to the flow of oxidizer. This feature eliminates the risk of explosions due to the formation of cracks within the solid grain, as can occur in

solid propellant engines.

One of the first analytical and experimental investigations on hybrid rocket engines was carried out by George Moore and Kurt Berman at the General Electric Company in Schenectady, New York, between the late 1940s and 1956. Their research program was based on a hypergolic hybrid propulsion system that used 90% concentrated hydrogen peroxide as an oxidizer and polyethylene as fuel. The peroxide was decomposed in a catalytic bed consisting of a silver screen, while the solid fuel was configured in a tubular shape or according to a bar and tube geometry. (Fig. 2.1).

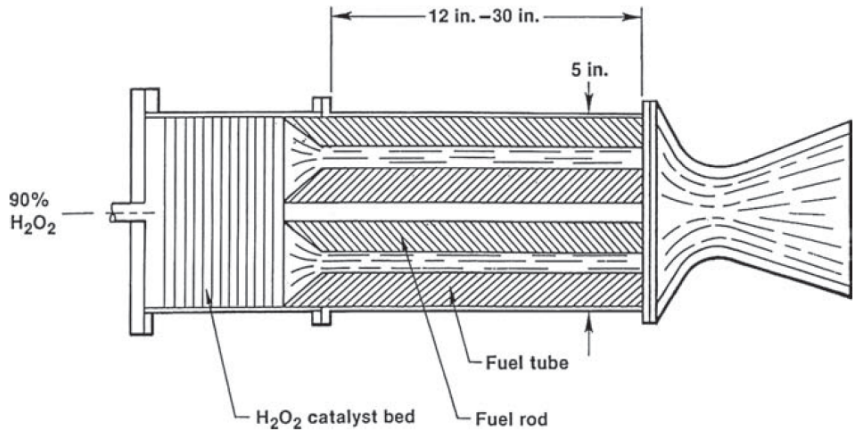

Figure 2.1: Diagram of the hybrid engine tested by Moore and Berman at General Electric. [2]

The purpose of this approach was to improve the performance of peroxide as a monopropellant. The experimenters observed that, by adding a relatively small amount of fuel (about 15% by mass compared to the propellant), the specific impulse increased by 70%, from 136 s to 230 s. This increase was facilitated by a slight extension of the combustion chamber between the catalytic bed and the nozzle.

Over 300 tests were conducted, including about 100 with the bar and tube configuration. From the experimental campaign, the authors drew the following main conclusions: combustion developed uniformly along the engine axis; cracks in the solid grain did not affect the combustion process; no starting difficulties were detected; combustion was stable because the fuel surface acted as a flame holder; flow restriction could be easily controlled by a single valve; finally, a high liquid/solid ratio promoted more uniform combustion in the chamber.

On the other hand, the researchers noted that the intrinsic thermal instability of peroxide was a problem and that it was difficult to modulate the combustion rate. The authors' observations were largely corroborated in subsequent years.

In 1952, William Avery and colleagues at the Johns Hopkins University Applied Physics Laboratory conducted tests on a "reverse" hybrid rocket propellant system. The propellants included benzene and jet fuel (JP), with solid oxidizers such as potassium perchlorate, ammonium nitrate, and ammonium perchlorate. The authors focused on the ammonium nitrate system because it was probably the cheapest option available, but the combination proved difficult to burn: the main problems encountered were uneven combustion and rather poor performance. The liquid/solid (oxidizer/fuel) ratio was approximately 0.035, which is about 200 times lower than the values used by Moore and Berman.

Reverse hybrid versions were also studied by Thiokol and the United Technologies Center (UTC) in the mid-1960s, using liquid hydrazine-based fuels and solid oxidizers such as perchlorates or hydrazinium salts. The solid charges were pressed, usually using a non-reactive fluorocarbon as a binder. However, these developments were gradually abandoned due to suboptimal combustion behavior and limited performance gains, which did not justify the complexities associated with pressing and handling solid charges.

2.2.2 Technological Maturation (1960–1990)

In the mid-1960s, a series of studies sponsored by NASA began, aimed at developing high-energy engines for space use. One of the concepts proposed was based on the use of lithium, hydrogen, and fluorine. Thanks to the intrinsic flexibility of hybrid propellants, lithium was incorporated into a grain of HTPB, while fluorine was mixed with oxygen in a solution called FLOX, composed of approximately 70% fluorine. This configuration optimized hydrocarbon combustion: oxygen reacted with carbon to form carbon monoxide (CO), while fluorine combined with hydrogen and lithium, ensuring high overall efficiency. The system achieved a specific impulse efficiency of 93%, corresponding to approximately 380 s in a vacuum.

A second approach, also developed under a NASA contract, was based on a combination of beryllium, oxygen, and hydrogen. In this case, the energy released by the combustion of beryllium was used to heat hydrogen (H_2). The concept involved incorporating beryllium into a low thermal conductivity binder, capable of providing the fuel grain structure required for hybrid operation. The addition of beryllium allowed for an increase in specific impulse of approximately 80%, equal to 65 s compared to the reference systems.

During the same period, several European organizations also launched similar programs. ONERA (Office National d'Études et de Recherches Aérospatiales) in France and Volvo Flygmotor in Sweden developed sounding rockets based on hybrid propulsion technology. ONERA focused its activities on a hypergolic rocket that used nitric acid as an oxidizer and amines as fuel. Eight flights were carried out: the first in April 1964, three in June 1965, and the last four in 1967, reaching

a maximum altitude of 100 km. The Volvo Flygmotor group used a propellant mixture similar to that of ONERA, but with Tagaform (polybutadiene with an aromatic amine) as fuel. The experimental flight was carried out in 1969, reaching an altitude of 80 km with a payload of 20 kg.

Meanwhile, the United Technologies Center (UTC), in collaboration with Beech Aircraft, was developing a supersonic target drone called Sandpiper. The system used MON-25 as an oxidizer (a mixture consisting of 25% nitric oxide and 75% dinitrogen tetroxide, N_2O_4) and a fuel composed of polymethyl methacrylate (PMM) and magnesium. Six flights were carried out in 1968, one of which achieved a burn time of 300 s and a maximum altitude of 160 km.

The second iteration of the rocket, known as HAST, used an IRFNA–PB/PMM propellant combination and allowed for a larger payload, as well as good thrust control.

The next model, developed in the mid-1980s by the Chemical Systems Division in collaboration with Teledyne Aircraft, used the same type of propellant as the HAST.

In the following decade, the American Rocket Company (AMROC) developed the largest hybrid rocket engine ever built at that time. Between 1980 and 1990, several versions of the engine were produced: the first, tested at the Air Force Phillips Laboratory, generated a thrust of approximately 312,000 N for 70 s, using liquid oxygen (LOX) and polybutadiene with terminal hydroxyl radicals (HTPB) as propellants. The second version, called the H-250F, achieved a thrust of over 1,000,000 N [3].

In 1982, Korey Kline of the Environmental Aeroscience Corporation (eAc) conducted the first test of a hybrid engine powered by gaseous oxygen and rubber at Lucerne Dry Lake in California. Kline and eAc later conducted the first hybrid tests of the SpaceShipOne program, with positive results, at Mojave (California).

In 1994, the United States Air Force Academy (USAF Academy) launched a hybrid sounding rocket that reached an altitude of approximately 5 km. The 6.4 m long vehicle used HTPB and LOX as propellants, providing a maximum thrust of 4,400 N for a duration of 16 s.

2.2.3 Academic and Industrial Revival (1990–2010)

Numerous universities have also contributed significantly to the development of hybrid rockets. In particular, research conducted by the Space Propulsion Group (SPG), led by Professor Arif Karabeyoglu at Stanford University, since 1999 has led to the development of a new class of liquefying fuels, including paraffin, characterized by high regression rates and excellent performance in terms of cost, availability, and reduced environmental impact.

In parallel with the activities of the Space Propulsion Group, other research

centers launched new development programs dedicated to hybrid propulsion systems, with the aim of gaining a deeper understanding of their combustion and regression mechanisms. In the United States, starting in the early 2000s, numerous tests were conducted in collaboration between Stanford University and NASA Ames Research Center as part of the HYDRA project, aimed at studying the use of paraffin-based liquefying fuels and LOX/paraffin mixtures on a suborbital scale. The experimental results confirmed the high regression rate and combustion stability of these propellants, laying the foundation for their adoption in subsequent space programs.

In Europe, during the same period, the HYFIRE program was launched at the University of Stuttgart, funded by the German Aerospace Center (DLR). This project focused on the experimental and numerical analysis of LOX/HTPB and LOX/paraffin systems, with the aim of validating predictive models of regression rate and heat transfer in the combustion chamber. The activities of the HYFIRE project contributed significantly to the definition of experimental correlations that are now widely used for the design and simulation of hybrid engines, consolidating academic interest in this type of propulsion.

These results have renewed interest in hybrid rocket technology, paving the way for innovative solutions and new-generation space applications.

2.2.4 Modern Era and Commercial Applications (2010–today)

Over the last two decades, interest in hybrid rocket engines has been gradually revived thanks to advances in numerical modeling, the development of new fuels, and increasing attention to safety and sustainability. Several companies and research centers have undertaken the development of hybrid systems for suborbital or light orbital missions, exploiting the potential of liquefying fuels and modern oxidizer injection systems.

Among the most notable projects are Virgin Galactic's hybrid engine, used in the SpaceShipOne and SpaceShipTwo vehicles, powered by dinitrogen oxide (N_2O) and HTPB; the Nucleus program by the Norwegian company Nammo, which demonstrated a LOX/paraffin propulsion system in flight in 2018; and the more recent HyImpulse SL1, developed in Germany, which uses the same propulsion combination for small orbital launchers. Further contributions also come from emerging companies such as Pythom Space, which develops reusable hybrid systems for low-cost commercial missions.

These developments mark the transition of hybrid propulsion from a predominantly experimental technology to a concrete solution for operational applications, thanks to its intrinsic safety, simplicity of construction, and thrust regulation capabilities.

In summary, the history of hybrid rocket engines shows a continuous evolution from the pioneering concept of the 1930s to modern commercial systems. The contemporary focus on cost reduction, reliability, and environmental compatibility has brought this technology back to the forefront, and today it represents one of the most promising alternatives for the propulsion of small space launchers.

Chapter 3

Fundamentals of Hybrid Rocket Engine Operation

3.1 Introduction

In hybrid rocket engines, as in liquid, monopropellant, and solid rocket engines, the energy required to produce thrust is obtained from the combustion of fuel and oxidizer. In hybrid engines, the two propellants are stored separately and in different phases: typically, the fuel is contained in a solid grain, while the oxidizer is managed in a liquid or gaseous form.

The oxidizer is injected at the end of the grain, sometimes through a pre-combustion chamber, which promotes its vaporization and facilitates its entry into the combustion port. This configuration allows the oxidizer to be distributed evenly along the port, improving combustion homogeneity and process stability.

The combustible gases resulting from the pyrolysis of the solid fuel react with the oxidant along the port and complete combustion in the afterburner chamber. The hot gases produced are then expelled through the nozzle, generating thrust (Fig. 3.1).

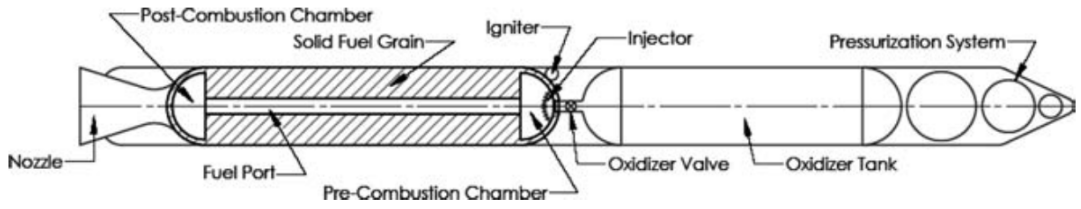

Figure 3.1: Diagram of a hybrid rocket engine. [2]

A key parameter influencing the design of solid grain and, consequently, the overall performance of the hybrid engine is the fuel regression rate, defined as the speed at which the solid material is converted into a gaseous phase.

In this type of rocket, combustion occurs mainly in the boundary layer that forms on the surface of the fuel, where the fluid phase oxidant comes into contact with the pyrolysis gases generated by the solid.

The term pyrolysis refers to the process of thermal decomposition of solid fuel, during which a phase change occurs accompanied by chemical reactions of molecular fragmentation, such as the breaking of polymer chains in the case of HDPE.

3.2 Advantages and Limitations

After analyzing the operating principle of hybrid propulsion, it is worth highlighting the positive aspects that have favored its development and use in space.

Compared to liquid propulsion, hybrid engines are distinguished by their greater *operational safety*. The separation of fuel and oxidizer significantly reduces the risk of explosions or catastrophic failures, while the solid nature of the fuel simplifies transport and storage operations.

Furthermore, the separation of the propellants makes the fuel grain inherently safer, as any internal imperfections or fractures do not significantly compromise the ballistics of the system. The resulting local increase in the combustion surface area has no critical effect on the overall behavior of the engine.

Compared to liquid rockets, hybrids require a less complex fuel system, as only one of the two propellants needs to be managed in fluid form. This leads to an increase in overall *reliability* and a reduction in the weight and mechanical complexity of the entire propulsion system.

The configuration of hybrid engines allows for a high degree of *maneuverability* and effective *thrust control*: thrust intensity can be varied continuously simply by modulating the oxidizer flow rate. This feature also allows for repeated start-ups and shutdowns (restarts) and offers the possibility of aborting a mission without destroying the propulsion system.

The presence of a solid phase allows the use of a wide range of additives, such as metal particles or catalysts, which can improve the performance of the propellant. In addition, the use of simple and readily available solid fuels helps to reduce production *costs* and the *environmental impact* of the propulsion system.

In conclusion, the flexible design of hybrid rockets allows them to be used in a wide range of missions: from launch boosters and upper stage propulsion to precision thrust systems for attitude maneuvers and orbit maintenance.

However, despite its many advantages, hybrid propulsion still has some limitations. These mainly include the low fuel regression rate, which is generally an order

of magnitude lower than that of solid rockets. Consequently, in order to generate a fuel flow rate sufficient to achieve the desired thrust, grain configurations with a large combustion surface area must be used. Such geometries require larger chambers, resulting in an unfavorable volumetric ratio. Nevertheless, the development of advanced solid fuels and innovative oxidizer injection techniques is gradually reducing this limitation.

Furthermore, due to the strong coupling between the oxidizer and fuel flow rates, the mixing rate within the combustion chamber varies over time. This variation is due to the progressive increase in the port area during grain regression, which leads to greater production of combustible gases and changes the flow conditions. This dynamic inevitably affects the stability and overall performance of the engine.

Finally, hybrid rocket engines have a different combustion process than liquid and solid ones, in which the mixing of reactants is generally more efficient. In liquid propellant engines, mixing occurs on a microscopic scale, typically on the order of the size of atomized fuel droplets, while in solid engines, the fuel and oxidizer are intimately mixed within the grain. In hybrid engines, on the other hand, combustion occurs mainly in a macroscopic diffusion flame zone (not premixed), a condition that limits the overall efficiency of the process and, consequently, the performance of the engine.

3.2.1 Regression Rate

Stationary hybrid combustion can be interpreted as a turbulent diffusive flame localized within the boundary layer that develops along the fuel wall. In this configuration, the reaction zone is extremely thin compared to the thickness of the boundary layer, since the characteristic times of chemical kinetics are much shorter than the transport times dominated by diffusion and turbulent motion. The assumption of an infinitely thin flame is therefore adequate to describe the heat transfer to the fuel surface [4].

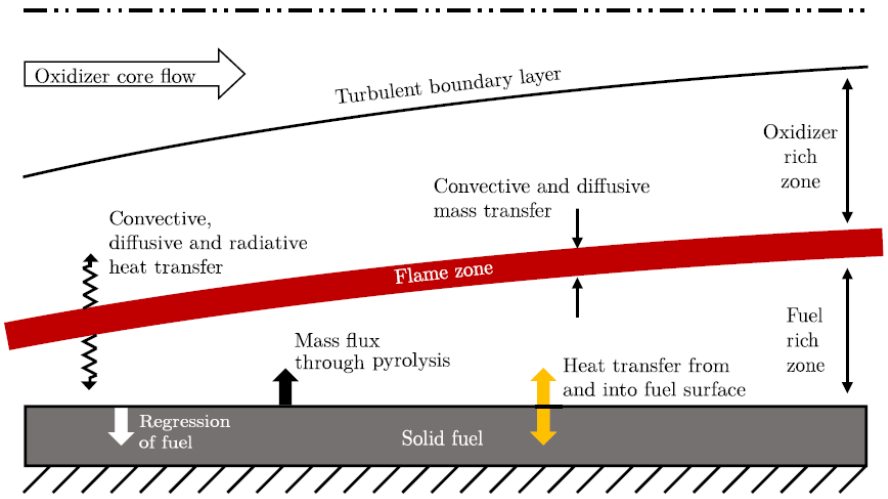

Figure 3.2: Simplified model of the boundary layer [5]

The total heat flux reaching the surface consists of convective and radiative contributions from the gas phase. Part of the incident heat is conducted into the fuel, while the remaining fraction feeds the pyrolysis processes and the consequent generation of gaseous products. Under steady-state conditions, the local energy balance at the surface can be expressed as

$$k\frac{\partial T}{\partial \eta} + \sum_{i=1}^{N} h_i \, \rho D_{im} \frac{\partial y_i}{\partial \eta} + \dot{m}_b h_s + \dot{q}_{\text{rad,abs}} = \dot{m}_b h_w + \dot{q}^{\text{ss}}_{\text{cond}} + \dot{q}_{\text{rad,em}} \tag{3.1}$$

The conductive term in the solid, assuming a one-dimensional model in a quasi-steady state, can be written as

$$\dot{q}^{\text{ss}}_{\text{cond}} = k_s \frac{\partial T_s}{\partial \eta} = \rho_s \dot{r} \, c_s (T_w - T_{si}) = \dot{m}_b \, c_s (T_w - T_{si}) \tag{3.2}$$

The quantity $\dot{m}_b h_s$ represents the enthalpy associated with the mass of fuel that regresses, while the radiative contributions include the absorbed flux $\dot{q}_{\text{rad,abs}}$ and the emitted flux

$$\dot{q}_{\text{rad,em}} = \varepsilon_w \sigma T_w^4$$

Introducing the effective heat of gasification,

$$h_v = \Delta h_p + c_s (T_w - T_{si}) \tag{3.3}$$

which includes both the energy required to heat the fuel to surface temperature and the heat required for pyrolysis processes, the energy balance can be rewritten in the classic form:

$$\dot{r} = \frac{\dot{q}_{\text{conv}} + \dot{q}_{\text{rad}}}{\rho_s h_v} \tag{3.4}$$

The expression (3.4) shows that the regression rate is proportional to the net heat flux incident on the surface and inversely proportional to the fuel density and the effective gasification heat. The result coincides with Marxman's classical formulation for regression in hybrid engines and highlights the high sensitivity of the model to pyrolysis heat values and the correct evaluation of heat fluxes.

3.3 Modeling of Pyrolysis and Combustion of Solid Fuel (HDPE)

3.3.1 Physical Description of the Combustion Process

In the case of a GOX/HDPE hybrid rocket, the gaseous oxidant flows along the grain port and develops a boundary layer of velocity, temperature, and composition. Convective transfer, possibly supplemented by radiation from the flame, heats the fuel wall until the thermal degradation of the polymer is activated.

The fuel does not change directly from solid to gas, but passes through two distinct regions:

- a *conduction zone*, in which heat propagates in the solid mainly by conduction along the surface normal;
- an extremely thin *surface pyrolysis zone*, in which the HDPE thermally degrades, producing gas.

The temperature in the conduction zone rises until it reaches a range where pyrolysis reactions become active. The gaseous products generated are expelled into the main flow, generating blowing and surface regression. The rate of regression depends on the balance between:

- convective and radiative heat flux to the surface,
- energy required to bring the fuel from T_{si} to T_w,
- energy required for pyrolysis processes (pyrolysis heat).

Radiative contribution

The energy balance at the surface also includes the radiative contribution, expressed as

$$\dot{q}_{\mathrm{rad,abs}} = \alpha_w \, \dot{q}_{\mathrm{rad}}, \qquad \dot{q}_{\mathrm{rad,em}} = \varepsilon_w \sigma T_w^4.$$

In the GOX/HDPE case, the radiative contribution is generally negligible compared to the convective contribution, since the combustion environment is free of particulates and highly radiative species. These conditions make the gaseous medium essentially transparent, and the radiative flux is often one or more orders of magnitude lower than the convective flux. Therefore, radiation can be treated as a secondary correction, useful for refining the local prediction of the heat flux but not decisive for the main regression mechanism.

3.3.2 Gas-Surface Interaction Model

HDPE combustion is represented by imposing a model on the fuel/gas boundary that respects the mass, species, and energy balances.

Global Mass Balance

$$\dot{m}_b = (\rho v)_w = \rho_s \dot{r} \tag{3.5}$$

where $\dot{m}_b$ is the total mass flux of pyrolysis products, ρ and v are the density and normal velocity in the gas at the wall, while ρ_s and $\dot{r}$ are the fuel density and regression rate.

Species Mass Balance

$$\rho D_{im} \frac{\partial y_i}{\partial \eta} + \dot{\omega}_i = (\rho v)_w \, y_i \tag{3.6}$$

where D_{im} is the species–mixture diffusion coefficient, y_i is the mass fraction, and $\dot{\omega}_i$ is the surface production rate due to pyrolysis.

Energy Balance

$$k \frac{\partial T}{\partial h} + \varepsilon_w \left(\dot{q}_{\mathrm{rad}} - \sigma T_w^4 \right) = \rho_s \dot{r} \left(\Delta h_p + c_s (T_w - T_{si}) \right) \tag{3.7}$$

Defining the effective gasification heat

$$h_v = \Delta h_p + c_s (T_w - T_{si})$$

the link between regression and net heat flux becomes

$$\dot{r} = \frac{\dot{q}_{\mathrm{conv}} + \dot{q}_{\mathrm{rad,net}}}{\rho_s h_v}. \tag{3.8}$$

3.3.3 HDPE Pyrolysis Model

The kinetics of HDPE pyrolysis are commonly described by a global reaction of the virgin polymer into gaseous products, modeled with first-order kinetics. The regression rate can be related to the surface temperature by

$$\dot{r} = \bar{A} \exp\left(-\frac{E_a}{2RT_w}\right) \tag{3.9}$$

where $\bar{A}$ is the pre-exponential factor (m/s), E_a is the activation energy, and R is the gas constant. The parameters $\bar{A}$ and E_a are obtained from experimental curves $\dot{r}(T_w)$ in controlled pyrolysis configurations. Table 3.1 shows the values adopted in Nasuti's work [6].

Surface Reaction	$\bar{A}$ [m/s]	E_a [kJ/mol]
HDPE $\rightarrow$ C_2H_4	4.78×10^3	251.04

Table 3.1: Arrhenius parameters for HDPE pyrolysis reported by Nasuti [6].

3.3.4 Gas Phase Combustion Model

The pyrolysis products of HDPE, mainly ethylene, mix with the oxidant in the port and chamber, generating gas phase combustion. Two main approaches are possible:

- *global* models, with few steps and suitable for describing the macroscopic evolution of the main species;
- *detailed* or *skeletal* mechanisms, with a greater number of species and reactions, more suitable for capturing flame structures and low-temperature chemistry.

In this work, three chemical mechanisms for ethylene oxidation were used: the detailed San Diego mechanism, Lu's skeletal mechanism, and Chang's reduced mechanism, in order to evaluate the uncertainty introduced by the choice of chemical model on thermo-fluid dynamic predictions.

3.4 Internal Ballistics

In hybrid engines, the fuel boundary layer, and therefore the regression rate, strongly depends on pressure, oxidant flow, and grain geometry. Experimental data show that the regression rate follows, in a first approximation, a power law with respect to the oxidant flow of the type:

$$r = a\, G_{ox}^{n}$$

Figure 3.3 shows the trend of the regression rate as the oxidant flow rate varies.

For intermediate mass flows, the regression behavior is dominated by turbulent heat transfer: in this regime, neither radiation nor chemical kinetics significantly influence the regression.

At high flow rates, the effect of convection becomes predominant, while at too low pressures the regression rate is limited by chemical kinetics. As the pressure increases, the reactivity of the propellant increases, increasing the regression rate.

However, if the flow rate is low, turbulent convection is relatively weak and the radiative contribution plays a dominant role.

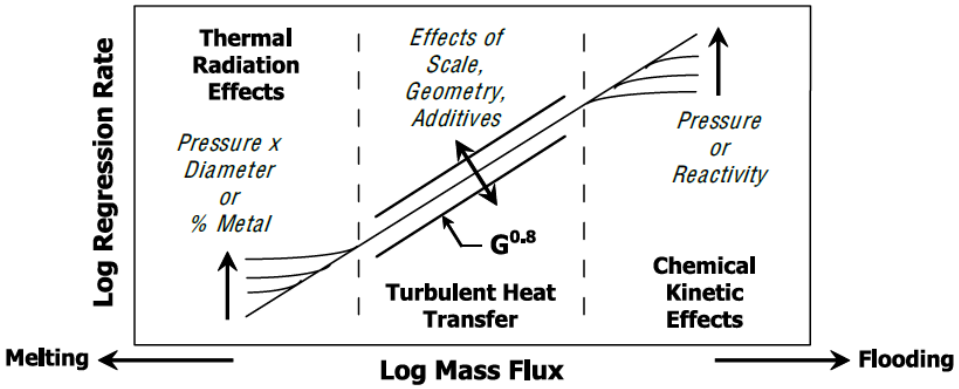

Figure 3.3: Regression rate dependence regime [2].

In addition to dependence on the oxidizing flow, the experimental data also show a clear correlation with chamber pressure. In particular, at the same oxidizing flow, an increase in pressure tends to increase the regression rate according to a relationship of the type:

$$r = a\, p_c^{n}$$

where a is the empirical regression coefficient and n is the exponent describing the sensitivity of the process to pressure. This dependence is linked to the increase in gas density and heat transfer efficiency to the wall, as well as to the increase in surface chemical reactivity. In general, an increase in pressure leads to more intense combustion and a higher regression rate.

The diameter of the port area also has a significant effect on engine performance. As pressure and internal diameter (pD) increase, the effect of radiation becomes predominant at high flow rates.

The term pD provides a measure of the optical density of the gas: when pD is high, the gas emits thermal radiation more efficiently, resulting in an increase in the regression rate.

Engine performance is also influenced by the amount of metal incorporated into the fuel. The addition of metals can have a beneficial effect on performance by increasing heat transfer, but at too low flow rates, combustion can become unstable or unsustainable [2].

In the literature, for fuels such as HDPE and paraffin, the coefficient a typically takes values between 10^{-4} and 10^{-3}

(per unit consistent with the system adopted), while the exponent n generally varies between 0.3 and 0.8, depending on the engine configuration and operating conditions [7].

These ranges reflect the strong coupling between convective, diffusive, and radiative phenomena in the hybrid combustion process.

Chapter 4

Numerical and Geometric Modeling

After describing the fundamental principles of hybrid combustion and the mechanisms that regulate fuel regression, it is appropriate to introduce one of the most significant contributions to the study of these phenomena: the work of Karabeyoglu et al. (2001–2005) [7].

The research conducted at the Stanford University Space Propulsion Group (SPG) represented a turning point in the study of liquefying fuels, such as paraffin, which are characterized by a higher regression rate than traditional polymeric fuels, such as HDPE.

In particular, Karabeyoglu developed a boundary layer flow model capable of describing heat and mass transfer in the presence of a surface liquid film, introducing a semi-analytical formulation for the fuel regression velocity and for the gas flow structure above the grain surface.

This model is now a widely validated reference case, used to compare numerical and experimental results obtained with different fuels and operating conditions.

In their work, Karabeyoglu et al. analyzed several cases of hybrid combustion, varying the type of fuel and operating conditions to evaluate the influence of the main parameters on the regression rate and flow pattern in the boundary layer. Among the cases tested, Test 1 was examined in this study, in which the fuel used was HDPE (High Density Polyethylene).

HDPE was chosen because its combustion follows pyrolysis and heat transfer mechanisms that can be fully described by Karabeyoglu's theoretical model, making it an ideal case for numerical analysis of regression and the boundary layer.

Tables 4.1 and 4.2 show the main parameters of the case considered, which will be analyzed in the following sections.

Test	Formulation	Initial Port ID (mm)	Oxidizer Flow Rate (g/s)	Final Port ID (mm)	O/F	Regression Rate (mm/s)	Ave. Oxidizer Flux ($g/cm^2 \cdot s$)	Chamber Pressure (atm)
1	HDPE	12.8	45.4	17.0	4.41	0.692	26.1	12.5
2	HDPE	17.0	45.3	20.1	4.87	0.522	16.8	11.8
3	HDPE	22.0	32.8	24.3	5.87	0.381	7.7	7.2
4	HDPE	12.8	32.9	16.2	3.79	0.568	19.9	9.6
5	Marcus 200	22.0	21.8	26.2	2.45	0.714	4.8	5.5
6	Marcus 200	22.1	43.9	27.8	3.23	0.945	9.9	11.5
7	Marcus 200	16.2	38.5	22.5	3.80	0.718	10.8	11.8
8	Marcus 200	15.7	41.0	24.3	2.70	1.428	13.1	10.6
9	PolyFlo 200	22.0	21.1	26.3	1.63	0.935	4.4	5.6
10	PolyFlo 200	22.0	39.9	30.4	1.70	1.400	7.4	10.3
11	PolyFlo 200	17.2	43.0	25.5	1.68	2.393	12.3	11.5
12	Paraf. FR4550	24.0	26.1	31.0	1.34	1.293	4.3	7.0
13	Paraf. FR4550	22.4	47.1	33.9	1.77	1.918	7.6	–
14	Paraf. FR4550	14.3	47.1	30.7	1.48	2.737	11.9	–

Table 4.1: Summary of motor test data (a).

Test	Formulation	Grain Length (cm)	Burn Time (s)	Nozzle Throat Diam. (mm)	Fuel Mass Burned (g)	Notes
1	HDPE	30.48	3.0	9.78	30.9	Successful Test
2	HDPE	30.48	3.0	9.78	27.9	Successful Test
3	HDPE	30.48	3.0	9.53	17.6	Successful Test
4	HDPE	30.48	3.0	9.91	26.0	Successful Test
5	Marcus 200	17.15	3.0	9.65	26.6	Successful Test
6	Marcus 200	17.15	3.0	9.65	40.7	Successful Test
7	Marcus 200	17.15	3.0	9.65	53.3	Successful Test
8	Marcus 200	17.23	3.0	9.96	45.5	Successful Test
9	PolyFlo 200	17.02	3.0	9.53	38.6	Successful Test
10	PolyFlo 200	17.02	3.0	9.53	70.2	Successful Test
11	PolyFlo 200	17.22	3.0	9.14	76.8	Successful Test
12	Paraf. FR4550	17.10	3.0	9.14	58.4	Successful Test
13	Paraf. FR4550	17.10	3.0	9.14	79.9	Pressure Trans. Failure
14	Paraf. FR4550	17.10	3.0	9.14	95.5	Pressure Trans. Failure

Table 4.2: Summary of motor test data (b).

4.1 Preliminary CEA (NASA) Analysis

Before proceeding with the numerical modeling of combustion, a preliminary analysis was carried out using NASA's *Chemical Equilibrium with Applications* (CEA) software [8]. The objective was to estimate preliminary data on the reaction between the fuel and the oxidizer, which would be useful as a reference for the subsequent evaluation of the CFD results.

In particular, the equilibrium flame temperature, the characteristic velocity c^*, the density, and the composition of the combustion products were determined.

A rocket-type simulation was then started under conditions of chemical equilibrium. The chamber pressure, propellant composition, and O/F mixture ratio corresponding to case 1 in Table 4.1 were entered as input data.

The main results are shown in Table 4.3.

	CHAMBER	THROAT	EXIT
p (bar)	12.666	7.3534	1.0132
T (K)	3499.68	3351.39	2894.01
ρ (kg/m^3)	1.1146	0.68669	0.11574

Table 4.3: CEA analysis results

4.2 Definition of the Physical Domain

The HDPE grain in case 1 has a length of 30.48 cm, an initial port diameter of 12.8 mm, and a final diameter of 17 mm. To adapt the geometry of the numerical model to the problem under consideration, we chose to assume an average value for the port area calculated between the initial and final values. The average area is therefore equal to:

$$A_{\text{average}} = 177.83 \text{ mm}^2$$

It was therefore necessary to model both the pre-combustion chamber and the post-chamber in order to correctly reproduce the flow and mixing conditions throughout the entire engine domain.

4.2.1 Mixing Chamber

Inside hybrid rockets, oxidizer and fuel are not premixed. During combustion, the vaporized fuel detaches from the grain surface and mixes with the oxidizer coming from the inlet.

However, this mixing does not occur instantaneously: in fact, regions locally rich in fuel or oxidizer may still be present at the end of the grain. For this reason, a mixing chamber is introduced downstream of the grain, with the aim of prolonging the residence time of the reactive gases and promoting the completion of mixing and combustion.

This measure reduces the fraction of unburned species, improves flow uniformity, and increases the overall efficiency and performance of the engine.

In order to estimate the volume of the mixing chamber, the characteristic length L^* was used, defined as:

$$L^* = \frac{V_c}{A_t}$$

In the absence of specific values in the literature for the GOX/C_2H_4 system, reference was made to the parameter relating to the LOX/RP-1 reaction, since both systems involve the combustion of hydrocarbons in the presence of oxygen. A characteristic length value of $L^* = 1$ m was therefore assumed [9].

This approach allows for a conservative estimate of the chamber volume, ensuring an adequate residence time for the completion of the mixing and combustion processes. However, the CFD analyses carried out a posteriori show that, for the configuration under consideration, the flow does not develop complete recirculation within the chamber; consequently, the volume adopted does not significantly influence the solution.

We can therefore write:

$$\tau^* = \frac{M}{\dot{m}} = \frac{\rho_c V_c}{\dot{m}} = \frac{\rho_c V_c \; c^*}{p_c A_t} = \frac{L^* \; c^*}{R T_c \; A_t}$$

With the results obtained from the simulation carried out using the CEA (Tab. 4.3) and those provided by Karabeyoglu (Tab. 4.1 and Tab. 4.2), it was possible to determine the volume of the mixing chamber $V_c = 7.51 \; 10^{-5} \; m$.

The diameter was assumed to be:

$$D_{MC} = 3 \; D_m = 45 \; mm$$

Subsequently, the convergent nozzle connection was designed following the guidelines provided in the exercises of the course “Endoreattori” (Rockets), “Dimensionamento Ugelli” (Nozzle Sizing) by Prof. Filippo Masseni [10].

The profile was defined by imposing a regular curvature between the combustion chamber and the throat, in order to ensure a gradual acceleration of the flow and minimize losses due to possible boundary layer separation.

The divergent nozzle was then truncated shortly after the throat, limiting the overall length to only the section necessary to ensure the correct initial expansion of the flow.

4.2.2 Pre-Chamber

The pre-chamber performs a fundamental function of stabilizing and preparing the oxidizing flow before it comes into contact with the solid fuel inside the port. In the absence of this component, the oxidizer would tend to distribute unevenly along the grain, causing irregular combustion and a consequent reduction in overall engine performance.

Furthermore, the volume of the pre-chamber allows for the damping of turbulence and residual vortices coming from the injection system, promoting flame front stability and a more uniform flow at the combustion chamber inlet.

Once the external diameter of the engine was determined, a ratio of $L/D = 0.5$ was adopted, as suggested in the literature [11], in order to obtain the overall length of the chamber.

4.3 Mesh Generation

The domain was discretized using an axisymmetric 2D mesh generated in ANSYS Meshing.

A structured *quadrilateral dominant* grid was adopted, with a characteristic length of 0.001 m, in order to accurately capture the main fluid dynamic phenomena within the domain.

Particular attention was paid to refinement near the fuel surface and chamber walls, where the velocity and temperature boundary layers develop. A growth rate of 1.1 with 12 cell layers was used to ensure correct resolution of the viscous sublayer.

The mesh check returns a *Minimum Orthogonal Quality* of 0.359 and a *Maximum Aspect Ratio* of 13.54.

Furthermore, the mesh consists of 10,231 cells, 20,905 faces, and 2,908 nodes, for a total volume of 1.892 10^{-4} m^3.

Figure 4.1: Mesh

Figure 4.1 shows the mesh obtained for the calculation domain.

4.4 Boundary Conditions

The domain is delimited by several boundary areas, which include the oxidizer inlet, the fuel inlet, the outlet, the axis of symmetry, the engine wall, and the grain

wall.

Each boundary was defined and modeled within ANSYS Fluent with the aim of accurately describing the actual operating and geometric conditions of the rocket.

An operating condition of zero was set in order to work with absolute rather than relative pressures.

The domain was defined as axisymmetric, assuming the $y = 0$ axis as the axis of symmetry.

4.4.1 Wall

The *Wall* category includes the walls of the rocket and the side walls of the fuel grain, as they do not participate directly in combustion.

This type of boundary condition requires:

- the *no slip condition*:

$$u_w = 0$$

- the *impermeability condition*:

$$\nu_w = 0$$

- *adiabaticity*:

$$\frac{dT}{dy} = 0$$

4.4.2 Oxidant Inlet (O_2)

The oxidant inlet was modeled as a *Mass flow inlet* in order to directly impose the desired mass flow rate.

The oxidant injection configuration was defined based on the approach adopted in the literature [12], in particular for the choice of inlet diameter and the conditions for introducing the gaseous oxygen flow.

The flow rate is:

$$\dot{m}_{ox} = 0.0454 kg/s$$

A total temperature of 300 K was also imposed.

Mass Flow Rate (kg/s)	0.0454
Supersonic/Initial Gauge Pressure (Pa)	101325
Turbulent Intensity (%)	5
Total Temperature (K)	300

Table 4.4: Boundary conditions O_2

4.4.3 Fuel Inlet (C_2H_4)

The fuel inlet was modeled as *Wall*, since it was necessary to impose the heat flow associated with the pyrolysis process of the solid fuel.

Consistent with the breaking of polymer chains and in accordance with the findings of Prof. F. Nasuti [6], it was assumed that the only product of HDPE pyrolysis is ethylene (C_2H_4).

Table 4.5 shows the thermophysical properties of HDPE used in the model:

Density ρ_s kg/m^3	Specific Heat c_s J/(kg K)	Thermal Conductivity k_s W/(m K)	Heat of Pyrolysis Δh_p MJ/kg
960	1255.2	0.1549	2.72

Table 4.5: HDPE properties [6]

Starting from the fuel flow rate reported in Table 4.2,

$$\dot{m}_f = 0.0103 kg/s$$

a uniform mass flow was imposed over the entire fuel surface equal to:

$$G_f = \frac{\dot{m}_f}{S_f} = 0.719 \text{ kg}/(\text{s} \cdot \text{m}^2)$$

In accordance with the same work, a negative heat flux equal to:

$$\dot{q}_{chem} = \dot{m}_f \Delta h_p \;\Rightarrow\; \dot{q}''_{chem} = \frac{\dot{m}_f \Delta h_p}{S_f} = 1.95\ 10^6\ W/m^2$$

representing the energy removed from the system by the pyrolysis process.

Material	HDPE
Species Mass Fraction / Mass Flux (kg/m^2 s)	0.719
Heat Flux (W/m^2)	-1.95 10^6

Table 4.6: Boundary conditions C_2H_4

4.4.4 Outlet

The outlet was treated as a *Pressure outlet*, imposing a static pressure of 11325 Pa, in order to ensure the correct functioning of the nozzle in supercritical conditions.

The possibility of flow re-entry into the domain was also disabled in order to avoid numerical instability and the formation of non-physical phenomena near the outlet.

Gauge Pressure (Pa)	11325
Prevent Reverse Flow	

Table 4.7: Boundary conditions C_2H_4

Chapter 5

Physical Modeling

Turbulence in high Reynolds number combustion problems can be addressed using models with different levels of fidelity. *Direct Numerical Simulation (DNS)* represent the most comprehensive approach, as they directly solve all turbulent scales using unsteady, three-dimensional Navier–Stokes equations. Due to the enormous computational requirements, they are only applicable to relatively simple configurations with Reynolds numbers in the range of 10^4–10^5.

To reduce computational costs without sacrificing an accurate description of turbulent structures, *Large Eddy Simulation (LES)* has been developed, which solves the larger energy scales by modeling the dissipative ones.

A further step towards reducing costs is represented by Reynolds-Averaged Navier–Stokes (RANS) models, discussed in the next chapter, in which all turbulence scales are modeled.

There are also hybrid approaches, such as Detached Eddy Simulation (DES) and Delayed Detached Eddy Simulation (DDES), which combine the benefits of RANS and LES by allowing direct resolution of large structures in the bulk of the flow and the use of RANS in regions near the wall. However, for large domains and turbulent combustion problems, the computational cost remains significant.

5.1 Reynolds-Averaged Navier-Stokes (RANS)

In CFD simulations of hybrid engines, the flow inside the combustion chamber is characterized by high turbulence, due both to the interaction between the oxidizing jet and the pyrolysis products coming from the fuel surface, and the presence of strong pressure and temperature gradients. However, the direct description of all turbulent scales using a DNS (Direct Numerical Simulation) would be computationally prohibitive.

To reduce the computational cost while maintaining a realistic representation

of the phenomena, the RANS (Reynolds-Averaged Navier–Stokes) approach is adopted . In this formulation, the Navier–Stokes equations are averaged over time by decomposing the variables into an average component and a fluctuating component:

$$u(x,t) = \overline{u}(x) + u'(x,t) \tag{5.1}$$

5.1.1 Average

Depending on the nature of the problem, different types of averages can be adopted. For incompressible flows, the following are commonly used:

- *time average* if the problem is statistically stationary:

$$\overline{u}(x) = \lim_{T\to\infty} \frac{1}{T} \int_t^{t+T} u(x,t)\ dt$$

- *spatial averaging* if the problem is statistically homogeneous in space:

$$\overline{u}(t) = \lim_{\Omega\to\infty} \frac{1}{|\Omega|} \int_\Omega u(x,t)\ d\Omega$$

  where Ω is the integration volume.

- *ensemble mean* for generic turbulence problems, which are non-homogeneous and non-stationary:

$$\overline{u}(x,t) = \lim_{N\to\infty} \frac{1}{N} \sum_{n=1}^{N} u_n(x,t)$$

In the case of compressible flows, where density varies in time and space, mass- or pressure-weighted averages are used. The most common approach is:

- Favre average weighted with respect to density

$$\widetilde{u}(x) = \frac{1}{\overline{\rho}} \lim_{T\to\infty} \int_t^{t+T} \rho(x,t)u(x,t)\ dt$$

5.1.2 Properties of the Averaging Operator

Mean operators are a fundamental tool for the analysis of turbulent flows, as they allow the mean components to be separated from the fluctuating components of physical quantities. Let us consider the Reynolds mean operator.

For all formulations based on this approach, the mean of the fluctuating part is zero:

$$\overline{u'(x,t)} = 0 \tag{5.2}$$

However, the average of the product of two fluctuating components is not zero, as it represents the correlation between the fluctuations themselves:

$$\overline{u_i' u_j'} \neq 0 \tag{5.3}$$

5.1.3 Reynolds Averaged Equations (RANS)

Applying Reynolds decomposition to the Navier–Stokes equations with Favre averaging, we obtain the following system of equations for the mean variables:

- **Continuity equation**:

$$\frac{\partial \overline{\rho}}{\partial t} + \frac{\partial}{\partial x_i}\left(\overline{\rho}\widetilde{q_i}\right) = 0 \tag{5.4}$$

- **Momentum equation**:

$$\frac{\partial \overline{\rho}\widetilde{q_i}}{\partial t} + \frac{\partial}{\partial x_j}\left(\overline{\rho}\widetilde{q_i}\widetilde{q_j}\right) = -\frac{\partial \overline{p}}{\partial x_i} + \frac{\partial}{\partial x_j}\left(\overline{\tau_{ij}} - \widetilde{\rho q_i' q_j''}\right) \tag{5.5}$$

  where $\overline{\rho q_i' q_j'}$ represents the Reynolds stresses, which introduce new unknowns into the averaged equations that must be closed using turbulence models. In the case of Favre averaging, the Reynolds stress tensor takes the form:

$$\tau_{ij}^F = \overline{\rho}, \widetilde{q_i' q_j''} \tag{5.6}$$

- **Energy equation**:

$$\begin{aligned}\frac{\partial}{\partial t}\left(\overline{\rho}\widetilde{E}\right) + \frac{\partial}{\partial x_j}\left[\overline{\rho}\widetilde{q_j}\left(\widetilde{E} + \widetilde{K}\right)\right] = &-\frac{\partial}{\partial x_j}\left(\tilde{q}_j\,\overline{p}\right) + \\ &+ \frac{\partial}{\partial x_j}\left(\widetilde{K}\frac{\partial \widetilde{T}}{\partial x_j} - \overline{\rho}\,\widetilde{q_j' h''} + \widetilde{\tau_{ij} q_i''} - \overline{\rho}\,\widetilde{q_j' K}\right) + \\ &+ \frac{\partial}{\partial x_j}\left[\widetilde{q_i}\left(\widetilde{\tau_{ij}} - \overline{\rho}\,\widetilde{q_i'' q_j''}\right)\right]\end{aligned} \tag{5.7}$$

The quantities $\overline{\rho q_i' q_j'}$, $\widetilde{E}$ and $\widetilde{K}$ require model closure, obtained using turbulence models such as the k–ω or SST model, used in *Fluent*, which will be discussed later.

5.1.4 Boussinesq Model

A model is introduced for approximating the stress tensor τ_{ij}^F that allows the system to be closed.

The tensor is divided into two components, one anisotropic and one isotropic.

We can write:

$$\tau_{ij}^F = 2\mu_t \widetilde{S_{ij}} - \frac{2\mu_t}{3}\frac{\partial \widetilde{q_k}}{\partial x_k}\delta_{ij} - \frac{2}{3}\overline{\rho} k \delta_{ij} \tag{5.8}$$

where μ_t is the turbulent viscosity, $\widetilde{S_{ij}}$ is the average strain tensor, calculated with the Favre-averaged velocity:

$$S_{ij} = \frac{1}{2}\left(\frac{\partial \widetilde{q_i}}{\partial x_j} + \frac{\partial \widetilde{q_j}}{\partial x_i}\right)$$

k is the turbulent kinetic energy:

$$k = \frac{1}{2}\overline{q_i' q_j'}$$

and δ_{ij} is the Kronecker delta.

The first term represents the anisotropic component of the Reynolds stress tensor, while the second and third terms constitute the isotropic part, which in the case of incompressible flows can be neglected.

5.2 Models for Turbulent Viscosity

After introducing turbulent viscosity μ_t, it is necessary to define its expression. To close the system of Reynolds equations, empirical or semi-empirical models based on one or two transport equations are used.

In single-equation models, turbulent viscosity is determined by solving an additional equation, usually for *turbulent kinetic energy* k. In two-equation models, on the other hand, two differential equations are solved: one for k and one for a second variable that describes the time or dissipation scale of turbulence, such as the *turbulent dissipation rate* ε or the *specific dissipation* ω.

The most commonly used two-equation models are the $k-\varepsilon$ model, the $k-\omega$ model, and the SST (*Shear Stress Transport*) model, which combines the two previous ones.

The SST model was adopted for the simulations conducted.

5.2.1 $k - \varepsilon$ Model

As already mentioned, two transport equations are introduced in the k–ε model: one for turbulent kinetic energy k and one for turbulent dissipation rate ε.

In the case of compressible flows, the two equations are rewritten in conservative form, multiplying each by the mean density $\overline{\rho}$.

The transport equation for $\overline{\rho}k$ takes the form:

$$\frac{\partial\left(\overline{\rho}k\right)}{\partial t}+\frac{\partial\left(\overline{\rho}\widetilde{q_i}k\right)}{\partial x_i}=\frac{\partial}{\partial x_j}\left[\left(\mu+\frac{\mu_t}{\sigma_k}\right)\frac{\partial k}{\partial x_j}\right]+G_k-\overline{\rho}\varepsilon+Y_M \tag{5.9}$$

where:

- the first term represents the temporal variation of k;
- the second describes convective transport;
- the diffusive term on the right side of the equal sign takes into account the contribution of molecular viscosity μ and turbulent viscosity μ_t, modulated by the empirical coefficient σ_k;
- G_k represents the production of turbulent kinetic energy, and is generally assumed to be:
$$G_k=\tau_{ij}^F\frac{\partial\widetilde{q_j}}{\partial x_i}$$
- $\overline{\rho}\varepsilon$ is the dissipation term and represents the rate at which turbulent kinetic energy is transferred from larger scales to smaller scales;
- Y_M introduces the effects due to the compressibility of the flow. It is usually modeled as:
$$Y_M=2\overline{\rho}\varepsilon M_t^2 \tag{5.10}$$
where M_t is the turbulent Mach number $M_t=\frac{\sqrt{k}}{a}$;

We proceed in a similar way to write the equation for the *turbulent dissipation rate* ε:

$$\frac{\partial\left(\overline{\rho}\varepsilon\right)}{\partial t}+\frac{\partial\left(\overline{\rho}\widetilde{q_i}\varepsilon\right)}{\partial x_i}=\frac{\partial}{\partial x_j}\left[\left(\mu+\frac{\mu_t}{\sigma_\epsilon}\right)\frac{\partial\epsilon}{\partial x_j}\right]+C_{1\varepsilon}\frac{\varepsilon}{k}G_k-C_{2\varepsilon}\overline{\rho}\frac{\varepsilon^2}{k} \tag{5.11}$$

where:

- the first term represents the time derivative;
- the second term describes convective transport;

- the term on the right side of the equal sign is the diffusive term analogous to the equation described above;
- the term $C_{1\varepsilon}\frac{\varepsilon}{k}G_k$ represents the production term of ε;
- the term $C_{2\varepsilon}\overline{\rho}\frac{\varepsilon^2}{k}$ represents the destruction term of ε;

the terms $C_{1\varepsilon}$ and $C_{2\varepsilon}$ are empirical constants that influence the behavior of the model.

By integrating these two equations , we can evaluate the turbulent viscosity μ_t, which is fundamental for closing the model and for calculating the stress tensor using the linear Boussinesq model (Eq. (5.9)).

However, this model has some limitations. In the presence of laminar flow, $k \to \infty$, while ε remains finite, leading to the ratio $\varepsilon/k \to \infty$. For numerical implementation, it is therefore necessary to impose appropriate boundary conditions. Near the wall, where the adhesion condition must be respected, we assume $k = 0$. Consequently, the turbulent viscosity is zero at the wall:

$$\mu_t = \rho C_\mu \frac{k^2}{\varepsilon} = 0$$

This condition ensures that the wall remains an area free of turbulent fluctuations.

5.2.2 Wilcox $k-\omega$ Model

The k–ω model is similar to the model just described. The first transport equation concerns the turbulent kinetic energy k:

$$\frac{\partial\left(\overline{\rho}k\right)}{\partial t} + \frac{\partial\left(\overline{\rho}\widetilde{q_i}k\right)}{\partial x_i} = \frac{\partial}{\partial x_j}\left[\left(\mu + \frac{\mu_t}{\sigma_k}\right)\frac{\partial k}{\partial x_j}\right] + G_k - \beta^*\overline{\rho}\omega k \tag{5.12}$$

This model also includes a non-stationary term, a convective transport term, a diffusive term, and two production and destruction terms.

The second transport equation defines the *turbulent dissipation frequency* or *specific dissipation* ω, linked to the turbulent dissipation rate ε by the relation:

$$\omega = \frac{\varepsilon}{k} \tag{5.13}$$

The equation is written in the form:

$$\frac{\partial\overline{\rho}\omega}{\partial t} + \frac{\partial\left(\overline{\rho}\widetilde{q_i}\omega\right)}{\partial x_i} = \frac{\partial}{\partial x_j}\left[\left(\mu + \frac{\mu_t}{\sigma_\omega}\right)\frac{\partial\omega}{\partial x_j}\right] + \frac{\gamma\omega}{k}G_k - \beta^*\overline{\rho}\omega^2 + \frac{\overline{\rho}\sigma_d}{\omega}\frac{\partial k}{\partial x_j}\frac{\partial\omega}{\partial x_j} \tag{5.14}$$

where the terms indicate respectively:

- the time derivative;
- the convective term;
- the diffusive term;
- the production term;
- the destruction term;
- the cross-diffusion term, which relates the kinetic energy gradient to the specific diffusion gradient;

In this model, most of the coefficients are semi-empirical. Similar to the previous model, boundary conditions must also be imposed here. Specifically, those proposed by Wilcox are:

$$k = 0$$

$$\omega_{wall} = \frac{6\nu}{\beta_0 \, d^2} \tag{5.15}$$

where ν is the kinematic viscosity, d is the distance of the first grid point from the wall, and β_0 is the model constant.

It follows that:

$$\mu_t = \frac{\rho k}{\omega} \to 0$$

at the wall.

In addition, boundary conditions are imposed for the incoming turbulent kinetic energy. The *turbulent intensity* T_u is introduced, defined as:

$$T_u = \frac{q'}{|\mathbf{q}|}$$

where q' is the characteristic amplitude of the fluctuations and $|\mathbf{q}|$ is the modulus of the average inlet velocity. Relating this to k gives:

$$T_u = \frac{\sqrt{\frac{2}{3}k}}{\sqrt{\overline{q}_1^2 + \overline{q}_2^2 + \overline{q}_3^2}} = \frac{\sqrt{\frac{2}{3}k}}{\overline{q}} \tag{5.16}$$

In this way, it is possible to estimate k starting from a known value of turbulent intensity. Typically:

- $T_u \simeq 1\%$ for external flows;

- $T_u \simeq 5\%$ for LPT turbines;
- $T_u \simeq 10 - 20\%$ for HPT turbines;

Once k has been estimated, it is possible to obtain ω by introducing the *characteristic length of turbulence* l_T:

$$l_T = C\frac{k^{\frac{3}{2}}}{\varepsilon} = C\frac{k^{\frac{3}{2}}}{\omega k} = C\frac{\sqrt{k}}{\omega} \tag{5.17}$$

where C is an empirical constant and l_T can be estimated based on the geometry of the duct, in particular as a function of its diameter. Generally, $l_T = 10\%\ D$ is assumed.

5.2.3 SST Model

A widely used model in industry is the SST (*Shear Stress Transport*) model, proposed by Menter.

The idea behind this model stems from the observation that the $k - \omega$ model performs better in regions close to the wall and in the presence of flow separations, but is highly sensitive to the inlet conditions of the domain. The $k - \varepsilon$ model, on the other hand, is more robust with respect to boundary conditions, but less accurate in describing phenomena near the wall.

Menter proposed a hybrid model that combines the positive aspects of the $k - \varepsilon$ and $k - \omega$ models. The idea is to use the $k - \omega$ model in regions close to the wall, where it provides more accurate results, and the $k - \varepsilon$ model in more distant areas, where it is more stable and less sensitive to inlet conditions.

The equation of ε is therefore rewritten as a function of ω, using the relation (5.13). A blending function F_1 has also been introduced, which varies between 0 and 1 as a function of the distance from the wall, in order to obtain a weighted combination of the constants of the two models.

This achieves a continuous transition between the two formulations, maintaining the accuracy of the $k - \omega$ model in the wall regions and the robustness of the $k - \varepsilon$ model in the free-flow regions [13].

5.2.4 Wall y^+

The behavior of the solution near the wall strongly depends on the numerical resolution of the near-wall region. Near the wall, we can rely on boundary layer theory, which provides guidance on how to correctly represent the velocity profile. The parameters are normalized:

$$u^+ = \frac{u}{u_\tau} \qquad y^+ = \frac{y}{l_\tau}$$

where l_τ is the viscous length and u_τ is the viscous velocity at the wall, defined as:

$$u_\tau = \sqrt{\frac{\tau_w}{\rho}} \qquad \text{with} \qquad \tau_w = \mu \frac{\partial u}{\partial y}\bigg|_{wall}$$

Once u_τ has been determined, it can be verified that the grid is sufficiently refined in the near-wall region by requiring that the first cell center satisfy a value of y^+ of the order of unity, i.e., ($y^+ \approx 1$).

The variables u^+ and y^+ can be plotted on a bilogarithmic scale:

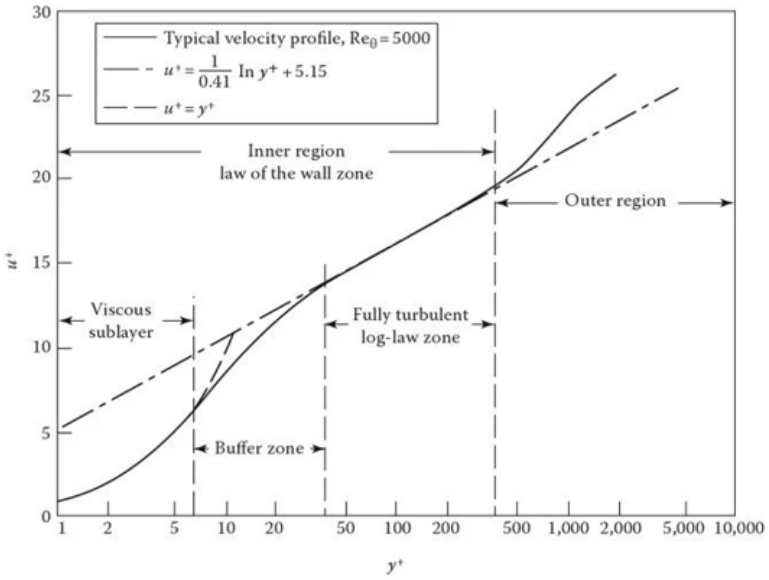

Figure 5.1: Behavior of the dimensionless variables u^+ and y^+

Three main regions can be distinguished in the flow near the wall:

- The *viscous sublayer* ($y^+ < 5$), where the linear relationship applies:

$$u^+ = y^+$$

- The *buffer layer* ($5 < y^+ < 30$), a transition zone in which no motion scale completely dominates.
- The *logarithmic zone* ($y^+ > 30$), which can be described by the wall law:

$$u^+ = \frac{1}{\kappa} \ln(y^+) + B$$

with $\kappa \approx 0.41$ Von Karman constant and $B \approx 5.2$ for canonical turbulent flows.

5.3 Reactive Flows

This section explores reactive flows, i.e., compressible and viscous flows in which chemical reactions occur.

These reactions play a fundamental role not only inside the combustion chamber, but also in other sections of the engine, such as air intakes and nozzles, where strong pressure and temperature gradients can alter the chemical composition of the gases during the expansion process.

Consider a compressible viscous reactive flow. Define N_S chemical species, each with a mass fraction y_i, such that:

$$\sum_{i=1}^{N_S} y_i = 1$$

We can therefore write N_S equations for the conservation of mass of each species:

$$\frac{\partial (\rho y_i)}{\partial t} + \nabla \cdot (\rho y_i \mathbf{q}) = -\nabla \cdot \mathbf{J}_i + \dot{\omega}_i \tag{5.18}$$

where:

- ρ is the density of the mixture;
- $\mathbf{J}_i$ is the diffusive term of the species;
- $\dot{\omega}_i$ is the production/destruction term of the i-th species;

The momentum equation takes the form:

$$\frac{\partial (\rho \mathbf{q})}{\partial t} + \nabla \cdot (\rho \mathbf{q}\mathbf{q}) = -\nabla p + \nabla \cdot \tau \tag{5.19}$$

where τ is the viscous stress tensor.
Finally, the internal energy of the mixture is calculated as:

$$\frac{\partial (\rho E)}{\partial t} + \nabla \cdot (\rho E \mathbf{q}) = \nabla \cdot (\sigma \mathbf{q}) - \nabla \cdot \mathbf{q}_T - \nabla \cdot \mathbf{q}_m \tag{5.20}$$

where:

- $\mathbf{q}_T$ represents the heat flux and can be written as:

$$\mathbf{q}_T = -k \nabla T \tag{5.21}$$

where k is the thermal conductivity;

- E is the total energy per unit mass, defined as:

$$E = e + \frac{1}{2}|\mathbf{q}|^2$$

in this equation e is the internal energy of the mixture and is defined as:

$$e = \sum_{i=1}^{N_S} y_i e_i \tag{5.22}$$

In turn:

$$e_i = h_i - \frac{p}{\rho}$$

and:

$$h_i(T) = h_i^\circ + \int_{T_0}^{T} c_{p,i}(T)\ dT$$

where:

  - h_i° is the standard enthalpy of formation of the i-th species at temperature T_0;
  - $c_{p,i}(T)$ represents the specific heat at constant pressure of the i-th species, expressed as a polynomial function of temperature according to the seven-coefficient NASA correlations ($NASA7$), also used in the software under consideration.

5.3.1 Mass Diffusion

Compared to the treatment of non-reactive flows, additional terms appear in the conservation equations.

In the mass conservation equation (Eq. 5.18) for individual species, there is a term related to *mass diffusion*. In the presence of a concentration gradient, chemical species tend to diffuse from regions of higher concentration to those of lower concentration.

The diffusive mass flow is described by Fick's law:

$$\mathbf{J}_i = -\rho\alpha_i \nabla y_i =$$

where α_i is the mass diffusivity of the i-th species.

It can also be written as:

$$\mathbf{J}_i = -\frac{\mu}{S_c}\nabla y_i$$

where μ is the dynamic viscosity and S_c is the Schmidt number:

$$S_c = \frac{\mu}{\rho \alpha_i}$$

This represents the simplest model for mass diffusion. However, there are more advanced models that take into account interactions between different species, thermodiffusion phenomena, and dependence on partial pressure gradients.

5.3.2 Energy Diffusion

Another important term is that associated with *energy diffusion*. In fact, during the diffusion process, each chemical species carries a certain amount of energy with it. Each species has a specific energy content that must be considered in the overall energy balance of the mixture.

This energy contribution can be expressed as:

$$\mathbf{q}_m = \sum_{i=1}^{N_S} \mathbf{J}_i \left(h_i^\circ + \int_{T_0}^{T} c_{p,i}(T)\ dT \right)$$

where the integral term represents the sensible enthalpy, i.e., the change in enthalpy due to temperature.

5.3.3 Production and Destruction of Species

The last term describes the chemical production and destruction $\dot{\omega}_i$, which appears in the mass transport equation for each chemical species.

This term represents the amount of species generated or consumed as a result of chemical reactions.

In the case of simple mixtures, the number of chemical reactions to be considered is limited. However, in more complex systems such as those based on HDPE, paraffin, or kerosene, the number of reactions increases significantly.

To manage this complexity, reduced chemistry models are used, which simplify the mechanism by retaining only the main reactions and the most chemically relevant species.

Given N_R chemical reactions, consider a generic reaction j involving a set of reactants and products:

$$\sum_{i=1}^{N_S} \nu_{i,j}^R B_i \rightleftharpoons \sum_{i=1}^{N_S} \nu_{i,j}^P B_i$$

where:

- B_i represents the i-th chemical species;

- $\nu_{i,j}^R$ is the stoichiometric coefficient of the i-th species among the reactants of the j-th reaction;
- $\nu_{i,j}^P$ is the stoichiometric coefficient of the i-th species among the products of the j-th reaction;

The expression of the production or destruction term $\dot{\omega}_i$, influenced by the stoichiometry and concentrations of the reactants, is:

$$\dot{\omega}_i = M_i \sum_{j=1}^{N_R} \left(\nu_{i,j}^P - \nu_{i,j}^R\right) \left(R_j^f - R_j^b\right)$$

where:

- M_i is the molecular weight of the i-th species;
- R_j^f is the forward reaction rate
- R_j^b is the backward reaction rate

The reaction rates are expressed as:

$$R_k^f = k_{f,j} \prod_{s=1}^{N_S} [C_s]^{\nu_{i,j}^R}$$

$$R_k^b = k_{b,j} \prod_{s=1}^{N_S} [C_s]^{\nu_{i,j}^P}$$

In this equation, $[C_s]$ is the molar concentration of species s:

$$[C_s] = \frac{\rho_s}{M_s}$$

while $k_{f,j}$ and $k_{b,j}$ are the kinetic coefficients of the forward and reverse reactions j. These are generally a function of temperature. A common formulation is the Arrhenius law, according to which:

$$k = A_j \, T^{n_j} \, e^{-\frac{E_a}{RT}}$$

where:

- A_j is the pre-exponential factor
- n_j is the temperature exponent;
- E_a is the activation energy;

- R is the universal gas constant;
- T is the absolute temperature.

At this point, a difficulty arises related to the different time scales characteristic of chemistry. In fact, the characteristic times of chemical reactions (τ_c) are generally extremely short. Compared to the typical time scales of fluid dynamics, this introduces a marked disparity in scale, which makes the system of equations highly stiff (*stiff*).

For this reason, convective and viscous terms in fluid dynamics tend to be treated with explicit methods, while chemical source terms are solved with implicit approaches. This strategy allows the numerical stability of the calculation to be maintained without having to excessively reduce the overall time step of the simulation.

5.4 Combustion Model

Once the behavior of a compressible, viscous, and reactive flow has been described, it is possible to model a laminar flame by directly solving the conservation equations, using a sufficiently fine spatial grid and an appropriately small time step.

However, when describing a turbulent flow, it becomes necessary to analyze the interaction between turbulence phenomena and chemical kinetics.

There are several strategies for describing the interaction between turbulence and chemical reactions. Among the main ones are the *Laminar Finite-Rate Model*, the *E*ddy Dissipation Model (EDM), hybrid models, the Beta-PDF Model, and the Flamelet Generated Manifold (FGM).

ANSYS Fluent also offers additional formulations, including Finite Rate – No TCI and Eddy Dissipation Concept (EDC), which are particularly popular approaches in the modeling of turbulent reacting flames.

5.4.1 Laminar Finite-Rate Model

This approach is the most computationally intensive. In fact, if you have sufficient resources, you can use DNS (Direct Numerical Simulation) or LES (Large Eddy Simulation) simulations, which directly solve all turbulence scales and the chemical evolution of reacting species.

In the case of RANS simulations, however, it is not possible to explicitly resolve these interactions, and it is necessary to introduce a model that describes the coupling between turbulence and chemistry. In ANSYS Fluent, the Finite Rate – No TCI (No Turbulence–Chemistry Interaction) model assumes that chemical

reactions proceed solely as a function of the average values of the flow variables, ignoring turbulent fluctuations.

The Laminar Finite-Rate Model calculates chemical source terms using Arrhenius expressions, neglecting the effects of turbulent fluctuations. The model is accurate for laminar flames but generally inaccurate for turbulent flames due to the highly nonlinear nature of Arrhenius chemical kinetics. However, it can provide acceptable results in cases where the chemistry is relatively slow and the interaction between turbulence and chemical reactions is reduced, as is the case, for example, in supersonic flames [13].

5.4.2 Eddy Dissipation Model (EDM)

This model is mainly used for premixed flames, in which fuel and oxidizer are injected separately and combustion occurs after mixing is complete.

In the Eddy Dissipation model, it is assumed that the chemical reaction occurs very quickly and that the overall combustion rate is controlled by turbulent mixing rather than chemical kinetics. In other words, combustion is considered to be limited by mixing, rather than by the intrinsic speed of chemical reactions.

Most fuels are characterized by fast combustion chemistry; as a result, the overall reaction rate is determined by the timescale of turbulent mixing. In premixed flames, turbulence slowly mixes fuel and oxidizer in the reaction zones, where they burn rapidly. In premixed flames, on the other hand, turbulence slowly mixes cold reactants and hot products in the reaction regions, where the chemical process proceeds rapidly. In these cases, combustion is said to be mixing-limited, and the (often unknown) complexity of chemical kinetics can be neglected.

In ANSYS Fluent, the interaction between turbulence and chemistry is modeled using the approach proposed by Magnussen and Hjertager, known as the Eddy Dissipation Model (EDM). The net production rate of species i due to reaction r, $R_{i,r}$, is defined as the minimum (i.e., the limiting value) of the following two expressions:

$$R_{i,r} = \nu'_{i,r} \, M_{w,i} \, A \, \rho \, \frac{\varepsilon}{k} \min_{\mathcal{R}} \left(\frac{Y_{\mathcal{R}}}{\nu'_{\mathcal{R},r} \, M_{w,\mathcal{R}}} \right)$$

$$R_{i,r} = \nu'_{i,r} \, M_{w,i} \, B \, \rho \, \frac{\varepsilon}{k} \frac{\sum_P Y_P}{\sum_j^N \nu''_{j,r} \, M_{w,j}}$$

where:

- Y_P is the mass fraction of a product P;
- $Y_{\mathcal{R}}$ is the mass fraction of a reactant $\mathcal{R}$;

- $A = 4.0$ and $B = 0.5$ are empirical constants;
- k and ε represent, respectively, turbulent kinetic energy and its dissipation.

The reaction rate is therefore governed by the turbulent mixing time scale, defined as:

$$\tau_{mix} \sim \frac{k}{\varepsilon}$$

As in Spalding's Eddy Break-Up model, combustion proceeds whenever turbulence is present ($k/\varepsilon > 0$), without the need for an additional ignition source. This approach is generally adequate for unmixed flames, while in mixed flames it can lead to immediate combustion of the reactants as soon as they enter the calculation domain, even upstream of the flame stabilizer [13].

For simulations in which it is necessary to accurately represent the local kinetic structure within turbulent vortices, however, it is preferable to adopt the EDC (Eddy Dissipation Concept) model, described in the following paragraphs.

5.4.3 Hybrid Models (EDM + Finite-Rate)

This approach combines the effects of chemical kinetics and turbulence, taking into account both the characteristic reaction and mixing times. The basic idea is that the overall combustion rate is determined by the slower of the two processes:

$$\tau_{eff} = \max(\tau_{mix}, \tau_{chem})$$

where τ_{mix} represents the characteristic time of turbulent mixing and τ_{chem} that associated with chemical kinetics.

In this way, it is also possible to describe intermediate situations, in which combustion is neither completely premixed nor completely unmixed, but presents a degree of partial premixing.

The hybrid model, implemented in ANSYS Fluent as Finite-Rate/Eddy Dissipation, simultaneously calculates the reaction rate according to Arrhenius' law (kinetic control) and that imposed by turbulent mixing (mixing control), assuming the minimum of the two as the effective rate. This allows for a more realistic representation of the transition between chemically dominated and mixing-dominated regimes, ensuring greater accuracy in simulations of partially premixed flames.

5.4.4 Beta-PDF Model

This formulation is based on RANS simulations, which provide average values of flow quantities but no information on their fluctuations. To account for the local

variability of scalar properties (such as composition or temperature), a probability distribution for a scalar variable, generally the mixture fraction Z, is introduced.

Starting from experimental data or high-fidelity simulations (DNS or LES), a lookup table is constructed that correlates the reaction rate and other thermochemical quantities with the average value and local variance of the key variable.

The average production rate of species i is then evaluated as a weighted average over the probability distribution:

$$\langle \dot{\omega}_i \rangle = \int_0^1 \dot{\omega}_i(Z)\, P(Z), dZ$$

where Z is the mixture fraction and $P(Z)$ is the probability density function (PDF) assumed to be of beta type, capable of realistically representing the distributions limited between 0 and 1 typical of scalar quantities in turbulent flows.

This approach allows the turbulence-chemistry interaction to be modeled effectively even in the absence of direct resolution of fluctuations, significantly reducing the computational cost compared to high-fidelity simulations.

5.4.5 Flamelet Generated Manifold (FGM)

This method is mainly used for modeling premixed flames. The approach is based on the generation of a precomputed table, called a mainfold, which represents the solution of chemical reactions as a function of a progress variable c, defined as:

$$c = 0 \ \text{(only reactants)} \qquad c = 1 \ \text{(only products)}$$

The chemical equations are first solved in a one-dimensional system (*flamelet*), obtaining a set of solutions that describe the behavior of the species and temperature along the direction normal to the flame front. These solutions are then tabulated and, during the CFD simulation, interpolated as a function of the variable c and other local parameters.

The main advantage of this method is its remarkable computational efficiency, as it avoids solving the complete chemical kinetics in real time. However, its disadvantage is its dependence on the correct definition of the manifold and the advance variable, which must accurately represent the local chemical state to ensure accuracy in flame prediction.

5.4.6 Eddy Dissipation Concept (EDC)

The Eddy Dissipation Concept (EDC) model is an extension of the Eddy Dissipation Model (EDM), developed to include detailed chemical kinetics in turbulent flows. The basic assumption is that reactions occur within small turbulent structures, called fine scales, where velocity and composition fluctuations are most intense.

The characteristic length fraction of the fine scales is modeled as:

$$\xi = C_\xi \left(\frac{\nu\,\varepsilon}{k^2}\right)^{1/4}$$

where:

- ν is the kinematic viscosity,
- k is the turbulent kinetic energy,
- ε is its dissipation rate,
- C_ξ is the volume fraction, an empirical constant equal to 2.1377.

The volume fraction of fine scales is therefore given by ξ^{*3}. Within these structures, species react on a characteristic time scale defined as:

$$\tau^* = C_\tau \left(\frac{\nu}{\varepsilon}\right)^{1/2}$$

where $C_\tau = 0.4082$ is an empirical constant.

In ANSYS Fluent, combustion in fine scales is treated as a constant pressure reactor, whose initial conditions correspond to the average values of temperature and composition of the cell. Chemical reactions evolve for a time τ^* according to Arrhenius laws, and numerical integration is performed using the ISAT (In Situ Adaptive Tabulation) algorithm, which allows chemical calculations to be accelerated by up to two or three orders of magnitude, significantly reducing simulation times.

The source term in the conservation equation for species i is expressed as:

$$R_i = \frac{\rho(\xi^*)^2}{\tau^*\left[1-(\xi^*)^3\right]}\left(Y_i^* - Y_i\right)$$

where Y_i represents the mass fraction of species i after the reaction in the fine scales for a time τ.

The EDC model therefore allows detailed chemical mechanisms to be integrated into turbulent reacting flows, providing an accurate description of the turbulence-chemistry interaction. However, since these mechanisms are often numerically stiff and require costly integration, the use of EDC is recommended only in cases where the instantaneous chemistry assumption is not valid [13].

5.5 Chemical and Reaction Mechanism

A chemical mechanism describes, in detail, the set of elementary reactions that govern the combustion of a fuel-oxidizer system. Each elementary reaction involves specific reactants, products, and intermediate radicals, and is accompanied by a kinetic law characterized by a pre-exponential factor, a temperature exponent, and an activation energy. The set of these reactions constitutes a kinetic model capable of predicting the evolution of chemical species and the heat released during the combustion process.

The complexity of a mechanism depends on the number of species involved and the reactions that transform them. Extended mechanisms, such as AramcoMech or USC Mech II, include hundreds of species and thousands of reactions, ensuring high accuracy but requiring significant computational resources. Reduced or semi-detailed mechanisms, on the other hand, retain only the reactions essential to correctly reproduce the behavior of the majority species, temperature, and main radials, making them more suitable for CFD simulations where computational cost is critical.

The choice of chemical mechanism is therefore a compromise between accuracy, numerical robustness, and computational cost: extended mechanisms guarantee a faithful description, while reduced mechanisms allow for faster simulations while maintaining an acceptable error on the variables of interest (temperature, reaction heat, major species).

To this end, three different chemical mechanisms for ethylene oxidation have been implemented: San Diego, Lu, and Chang, in order to quantify the uncertainty associated with the description of combustion chemistry and verify its impact on the distribution of temperature, major species, and reaction heat term.

5.5.1 San Diego Mech (UCSD)

The San Diego kinetic mechanism, developed at the University of California San Diego, is based on a philosophy oriented towards the targeted selection of reactions that are truly decisive for combustion, with particular attention to high-temperature ignition phenomena, flame propagation, and detonative processes. The construction approach is progressive: it starts with simple systems and introduces only the essential species and elementary steps, avoiding the inclusion of secondary reaction pathways that would increase the uncertainty of the kinetic parameters without providing significant benefits. The result is a relatively compact structure, consisting of 57 species and 268 reactions, which ensures a good balance between chemical detail, predictive reliability, and computational sustainability, making it a valid alternative to more extensive mechanisms such as USC Mech II or AramcoMech.

In the case of ethylene oxidation, the model focuses on the fundamental reaction

pathways of C_1-C_2 chemistry. The initial reactions between ethylene and O/OH radicals, together with the subsequent transformation of vinyl, are the most sensitive steps and regulate both the speed of ignition and the structure of the flame. This approach gives the mechanism a good ability to reproduce ignition times at high temperatures and under pressurized conditions, with trends consistent with the main experimental datasets and performance comparable to USC Mech in diluted stoichiometric mixtures. However, some known trends remain, such as the underestimation of ignition delays at lower temperatures and a slight overestimation of flame speed near stoichiometry at low pressure.

Overall, the combination of compactness, numerical robustness, and accuracy under the most relevant conditions makes it a well-suited mechanism for use in CFD simulations involving ethylene combustion, as in the case of GOX–C_2H_4 hybrid systems [14] [15].

5.5.2 Lu (Reduced USC Mech II)

The reduced mechanism developed by Tianfeng Lu at the University of Southern California is one of the main kinetic formulations dedicated to the combustion of unsaturated hydrocarbons, in particular ethylene and acetylene. It is a skeletal mechanism obtained through the systematic reduction of the detailed USC II mechanism, maintaining the predictive capacity of the species and reactions most relevant to the ignition and flame propagation processes. The proposed version includes 32 species and 206 reactions, representing an effective compromise between accuracy and computational cost.

This mechanism has been widely used in DNS simulations of ethylene flames, a context in which the use of detailed kinetics would be prohibitive. It provides a reliable representation of the main chemical processes governing ethylene oxidation, making it suitable for non-premixed applications and for the study of ignition and extinction phenomena [16].

The reduction process underlying this model is based on the Directed Relation Graph (DRG) approach introduced by Lu and Law. This methodology allows the systematic identification of the species and reactions that most influence the chemical dynamics, evaluating the dependencies between species through a directed graph. Species with negligible influence are removed, controlling the error introduced in the thermochemical prediction. DRG is one of the most established tools for generating accurate and efficient skeletal mechanisms, as it allows for a significant reduction in the size of the detailed mechanism while preserving key quantities such as flame speed, reactive zone thickness, and thermochemical profiles [17].

5.5.3 Chang

The mechanism developed by Yachao Chang and colleagues represents a reduced formulation for the oxidation of n-decane, obtained through a decoupling methodology designed to cover typical engine operating conditions, from low to high temperature and pressure regimes. The approach separates the chemical description: an extremely simplified model for C2–C10 species is used to reproduce the ignition characteristics of heavy hydrocarbons, while H2/CO/C1 kinetics are treated in detail to ensure accuracy in estimating laminar flame speed and extinction strain. The resulting mechanism includes 40 species and 141 reactions. The authors provide extensive validation by comparing the model with experimental data available from shock tubes, rapid compression machines, jet-stirred reactors, and flow reactors over a wide range of temperatures (550–1800 K), pressures (1–80 bar), and equivalence ratios (0.5–2), as well as concentration profiles, flame velocity, and extinction strain in premixed and countercurrent flames. Finally, the mechanism is applied to multidimensional simulation of combustion in PCCI engines, showing good agreement with measurements and confirming the effectiveness of the decoupling approach for reducing heavy alkane oxidation mechanisms [18].

Chapter 6

Numerical Methodology

6.1 Solver Type

ANSYS Fluent offers two main solving technologies: the pressure-based solver and the density-based solver. Both can be used for a wide range of flows, although in some conditions one of the two may offer better performance in terms of convergence speed or ability to solve specific flow characteristics [13].

6.1.1 Pressure-Based Solver

The *pressure-based solver*, historically used for incompressible or weakly compressible flows, solves the continuity and momentum equations by coupling pressure and velocity. It is available in two variants:

- *Segregated*: the governing equations are solved sequentially and uncoupled, with corrections iteratively applied to the pressure;
- Coupled: the momentum and continuity equations are solved simultaneously in coupled form. This formulation, based on an implicit monolithic approach, significantly accelerates convergence compared to the segregated method, at the expense of greater memory consumption.

6.1.2 Density-Based Solver

The *density-based solver*, originally developed for high-speed compressible flows, simultaneously integrates the mass, momentum, and energy equations, using density as the primary variable linked to pressure. There are two formulations:

- *Explicit*: requires less memory but imposes smaller time steps to ensure numerical stability;

- *Implicit*: has broader stability characteristics and allows for faster convergence to steady state, while requiring greater computing power.

In general, the density-based method is more accurate in solving highly compressible flows or flows with shock waves, while the pressure-based method provides greater robustness and stability for slow or weakly compressible flows, such as those that develop in a combustion chamber.

6.2 Pressure-Velocity Coupling Solution Method

In the pressure-based solver, the continuity equation is reformulated to obtain a pressure correction equation, which is necessary to ensure consistency between the velocity field and the pressure field. Since velocities are defined at the centroids of the control volumes, Fluent applies the *Rhie–Chow* correction to avoid spurious pressure oscillations and ensure stable discretization of mass flows.

The pressure–velocity coupling can be managed using *segregated* algorithms, which solve the motion and pressure equations separately, or using the *coupled* approach, in which these equations are treated simultaneously within the same linear system.

Fluent provides the following schemes:

- *SIMPLE*: segregated reference scheme for steady-state simulations;
- *SIMPLEC*: more aggressive variant of SIMPLE, generally faster;
- *PISO*: suitable for transient calculations with rapid pressure changes;
- *Fractional Step (FSM)*: used in unsteady simulations with non-iterative integration;
- *Coupled*: fully coupled scheme that solves pressure and momentum simultaneously.

The SIMPLE, SIMPLEC, PISO, and Fractional Step algorithms follow a predictor-corrector structure: the momentum equation provides a preliminary velocity field that is subsequently corrected by the pressure. In contrast, the *Coupled* scheme simultaneously solves momentum and continuity equations, increasing numerical robustness in the presence of strong non-linearity, at the cost of higher computational expense [13].

In this work, the *Coupled scheme* was adopted, as it was found to be more suitable for simulating a motion field strongly coupled to the thermochemical phenomena typical of combustion processes. The use of the Coupled solver also favored the use of higher-order convective discretization schemes, mitigating the onset of numerical oscillations that are more likely with segregated approaches.

6.2.1 Coupled

The coupled approach has significant advantages over segregated methods. In steady-state simulations, it offers greater robustness and faster convergence times, while in unsteady-state simulations, it is particularly useful in the presence of suboptimal meshes or when relatively large time steps are used. Although the computational cost per iteration is higher, the faster reduction in residuals often leads to a shorter overall convergence time.

In segregated schemes, the momentum equations and the pressure correction equation are solved independently. This semi-implicit formulation slows down convergence, especially in conditions characterized by marked non-linearity or complex pressure fields.

The coupled scheme, on the other hand, solves the momentum and continuity equations simultaneously. Full coupling is achieved through implicit discretization of the pressure gradient terms and an implicit formulation of mass flow on the faces, which incorporates Rhie–Chow dissipative terms to avoid unphysical pressure oscillations. This configuration increases numerical stability and accelerates the convergence of solutions.

Furthermore, the coupled scheme is particularly suitable in the presence of strong thermodynamic variations due to chemical reactions and locally compressible regimes. Under such conditions, the simultaneous solution of pressure and momentum reduces the risk of instabilities associated with sharp temperature and density gradients, improving consistency between dynamic and thermochemical fields.

In the present study, the combination of reactive flow, high density variations, heat transfer to solid fuel, and pyrolysis process made the use of the Coupled scheme preferable, as it is more stable in regions characterized by strong thermal gradients and highly coupled chemical reactions.

6.3 Spatial Discretization

Spatial discretization transforms the conservation equations of the RANS model, species transport, and energy into a numerically solvable algebraic system.

ANSYS Fluent adopts the Finite Volume Method (FVM), in which the equations are integrated over each control volume.

$$\frac{\partial}{\partial t}\int_V U \, dV = -\int_{\partial V} \mathbf{F}\cdot\mathbf{n} \, dS \tag{6.1}$$

where V represents the control volume, ∂V its boundary, U the vector of conservative variables, and $\mathbf{F}$ the total flow through the surface, including convective and diffusive contributions.

Integration over each volume ensures the local conservation of physical quantities, while the evaluation of flows on the faces of the cell requires the use of appropriate interpolation schemes.

6.3.1 Convective Flows: Interpolation Schemes

For the discretization of convective terms, ANSYS Fluent provides several upwind schemes, including *First-Order Upwind* (FOU), *Second-Order Upwind* (SOU), *Power Law*, and *QUICK*. The choice of scheme significantly affects the quality of the solution, especially in the presence of strong velocity and temperature gradients, as in the case of reactive flows.

Numerical Strategy

In the early stages of the analysis, the First-Order Upwind scheme was used, thanks to its high robustness in the presence of significant non-linearities and flow fields that had not yet stabilized. The use of a first-order scheme limits the occurrence of spurious oscillations and promotes the progressive reduction of residuals.

Once a pre-convergent configuration was reached, characterized by regular behavior of the conservative variables, the convective scheme was replaced with the Second-Order Upwind scheme in order to increase the accuracy of the solution and reduce numerical diffusion. The transition to a higher order allows for a more accurate description of the gradients of velocity, temperature, and mass fractions, which are particularly relevant in reactive flows with high spatial variability.

This gradual approach is an effective compromise between initial stability and final accuracy, ensuring a reliable and physically consistent numerical solution.

First-Order Upwind

The *First-Order Upwind* (FOU) scheme is the simplest and most robust method for discretizing convective terms in the Finite Volume Method. The flow at the cell face is evaluated using the value of the variable associated with the donor cell, i.e., the one from which the flow is directed. This choice guarantees monotonicity and avoids spurious oscillations, which is especially useful in the early stages of the simulation.

The value of the scalar quantity ϕ at face f is approximated as:

$$\phi_f = \phi_{\text{upwind}}$$

where ϕ_{upwind} is selected based on the sign of the convective flow:

$$\phi_{\text{upwind}} = \begin{cases} \phi_P, & (\mathbf{u} \cdot \mathbf{n}_f) > 0 \\ \phi_N, & (\mathbf{u} \cdot \mathbf{n}_f) < 0 \end{cases}$$

The discretization of the convective term in the FVM takes the form:

$$\int_{\partial V} \phi \left(\mathbf{u} \cdot \mathbf{n}\right) dS \approx \sum_{f} \phi_{\text{upwind}} \left(\mathbf{u} \cdot \mathbf{n}_f\right) S_f$$

This scheme is numerically stable but introduces significant numerical diffusion, especially in the presence of strong gradients.

Second-Order Upwind

The Second-Order Upwind (SOU) scheme increases the accuracy of convective discretization by means of a linear reconstruction of the variable in the upstream cell. Compared to the first order, it reduces numerical diffusion, but requires a well-resolved gradient field and a good mesh quality.

The scalar quantity ϕ at face f is calculated as:

$$\phi_f = \phi_{\text{upwind}} + \nabla\phi_{\text{upwind}} \cdot \left(\mathbf{x}_f - \mathbf{x}_{\text{upwind}}\right)$$

where $\nabla\phi_{\text{upwind}}$ is the gradient in the upstream cell and $(\mathbf{x}_f - \mathbf{x}_{\text{upwind}})$ is the vector from the upwind cell center to the face.

The selection of the upwind value follows the same criterion as the FOU scheme:

$$\phi_{\text{upwind}} = \begin{cases} \phi_P, & (\mathbf{u} \cdot \mathbf{n}_f) > 0 \\ \phi_N, & (\mathbf{u} \cdot \mathbf{n}_f) < 0 \end{cases}$$

The discretized convective term becomes:

$$\int_{\partial V} \phi \left(\mathbf{u} \cdot \mathbf{n}\right) dS \;\approx\; \sum_{f} \left[\phi_{\text{upwind}} + \nabla\phi_{\text{upwind}} \cdot \left(\mathbf{x}_f - \mathbf{x}_{\text{upwind}}\right)\right] \left(\mathbf{u} \cdot \mathbf{n}_f\right) S_f$$

This approach allows for greater accuracy, but is more sensitive to local gradients and requires a sufficiently regular mesh.

6.3.2 Evaluation of Gradients and Diffusive Quantities

The discretization of diffusive terms in conservation equations requires an accurate estimation of the gradients of scalar and vector variables within the cells. In ANSYS Fluent, the gradient $\nabla\phi$ of a generic variable ϕ is used to reconstruct the values at the faces in convective terms, to calculate diffusive contributions, and to evaluate the velocity derivatives used in turbulent models.

Fluent provides three main methods for evaluating gradients:

- Green–Gauss cell-based,
- Green–Gauss node-based,

- Least-Squares cell-based.

In this work, the *Least-Squares cell-based* method was adopted, selected for its excellent compromise between accuracy and computational cost, particularly effective on unstructured and geometrically irregular meshes.

Least-Squares Cell-Based Method

The least-squares method assumes that the variable ϕ varies linearly in the vicinity of the reference cell. Considering a cell c_0 and the adjacent cells c_i, the variation of ϕ along the vector connecting the centroids can be approximated by:

$$(\nabla\phi)_{c_0} \cdot \Delta\mathbf{r}_i = \phi_{c_i} - \phi_{c_0} \tag{6.2}$$

where $\Delta\mathbf{r}_i$ is the vector from the centroid of cell c_0 to the centroid of cell c_i.

Writing an equation for each of the n adjacent cells, we obtain the system in compact form:

$$\mathbf{J}\,(\nabla\phi)_{c_0} = \Delta\phi \tag{6.3}$$

where $\mathbf{J}$ is a matrix dependent exclusively on the local geometry and $\Delta\phi$ is the vector of differences between the values of the variable in the adjacent cells and that of the central cell.

Since the system is typically overdetermined, Fluent solves it in the least squares sense using a Gram-Schmidt decomposition, obtaining weights W_{i0}^x, W_{i0}^y and W_{i0}^z associated with the adjacent cells. The gradient in cell c_0 is then given by:

$$(\phi_x)_{c_0} = \sum_{i=1}^{n} W_{i0}^x\,(\phi_{c_i} - \phi_{c_0}) \tag{6.4}$$

$$(\phi_y)_{c_0} = \sum_{i=1}^{n} W_{i0}^y\,(\phi_{c_i} - \phi_{c_0}) \tag{6.5}$$

$$(\phi_z)_{c_0} = \sum_{i=1}^{n} W_{i0}^z\,(\phi_{c_i} - \phi_{c_0}) \tag{6.6}$$

Reasons for the choice

On irregular or oblique meshes, typical of the three-dimensional geometries of ducts and combustion chambers, the *least-squares cell-based* method is an advantageous choice for gradient reconstruction. This approach guarantees accuracy comparable to the Green–Gauss node-based method, at a lower computational cost, while improving the reconstruction of values on faces in convective terms and reducing errors introduced by mesh skewness.

For these reasons, ANSYS Fluent uses it as the default method for calculating gradients.

In this work, it has been adopted for all RANS simulations with species transport, as it is more robust on grids characterized by geometric irregularities and strongly non-orthogonal cells. ANSYS, in fact, recommends its use as the default configuration in the Fluent Solver environment [13].

6.4 Time Integration

Once all the information necessary for evaluating the flows at the interfaces has been defined, time discretization can proceed.

The equation in integral form (6.1) is recalled and the average cell value is introduced

$$\overline{U} = \frac{1}{|V|} \int_V U \, \mathrm{d}V$$

obtaining the semi-discrete form:

$$\frac{\partial \overline{U}}{\partial t} = -\frac{1}{|V|} \sum_{j=1}^{N_f} \mathbf{F}_j \cdot \mathbf{n}_j \, \Delta S_j$$

where N_f is the number of faces of the control volume, $\mathbf{F}_j$ is the total flux through face j and $\mathbf{n}_j$ is the associated outgoing normal.

The above equation represents, for each control volume, an ordinary differential equation in time, in which the spatial dependence has been entirely traced back to the interface flows.

This ODE can be integrated in time using explicit or implicit schemes. In industrial CFD solvers, and in particular in Ansys Fluent, first- and second-order implicit schemes are used, which guarantee greater numerical stability and allow the use of relatively high time steps, both in the case of real transient simulations and in the context of the pseudo-transient method used to accelerate the convergence of steady-state simulations [13].

6.4.1 Explicit Methods

This class of methods has numerous advantages: it requires less memory, since it does not involve the solution of linear systems, it allows local updates of conservative variables, and it lends itself naturally to parallelization. Furthermore, implementation is relatively simple and the structure of the method is easily scalable.

On the other hand, explicit schemes are subject to the CFL stability constraint, which requires the time step to satisfy the relation:

$$\Delta t \leq \frac{\mathrm{CFL}\,\Delta x}{\lambda_{\max}} \tag{6.7}$$

where $\lambda_{\max}$ represents the maximum characteristic velocity of the problem (e.g., the maximum convective velocity or the maximum velocity of acoustic waves). It follows that as the spatial discretization Δx decreases, the time step must also decrease proportionally, making the method inefficient on very refined meshes.

Among the most common explicit schemes are the explicit Euler method and Runge-Kutta formulations, which belong to the family of more accurate multi-step or multi-stage methods. However, these methods are rarely used in industrial CFD solvers due to severe limitations on the time step and the computational cost associated with realistic simulations with refined meshes.

6.4.2 Implicit Methods

Implicit methods, unlike explicit methods, allow the use of much larger time steps due to their unconditional stability. This advantage makes them particularly efficient when real-time evolution is not the main objective, but convergence to a steady-state solution is desired.

However, these methods have significantly higher computational costs: at each time step, it is necessary to solve a large linear (or nonlinear) system, whose cost increases with the number of mesh cells and the degree of coupling of the equations. Furthermore, parallelization is more complex than with explicit schemes, since the processes must exchange information at each iteration to update the global variables, reducing the efficiency of distributed computing.

Due to these characteristics, implicit schemes are generally more suitable for solving *stationary problems*, in which the interest is to obtain the convergent solution directly without following a physical transient. This approach also includes the pseudo-transient method used in industrial solvers, where time advancement is introduced as a numerical artifice to stabilize and accelerate the convergence of the system.

6.4.3 Pseudo-Transient Method

In this work, simulations were conducted using the Ansys Fluent pressure-based solver, which adopts an implicit time scheme for solving conservation equations. This choice is imposed by the nature of the problem at hand: the presence of chemical kinetics, the strong coupling between momentum, energy, and species transport equations, and the need to ensure numerical stability on refined meshes

make the use of explicit schemes impractical, as they would require extremely small time steps due to the CFL constraint.

Since the goal of the simulations is to obtain a stationary solution of the motion and combustion field, the time scheme is not used to follow a real physical transient, but as a numerical tool to facilitate convergence. To this end, the pseudo-transient method was used, which introduces an artificial time advance to stabilize the system of equations and improve the iterative behavior in the initial stages of the solution. Once a pre-convergence phase was reached, it was possible to progressively increase the pseudo-transient time step and adopt higher-order spatial schemes to increase the accuracy of the final solution.

Chapter 7

CFD Simulations

7.1 Convergence and Residuals

Convergence assessment is a fundamental part of CFD simulations, as it ensures that the solution obtained is stable, physically consistent, and independent of the initial conditions.

Convergence is evaluated in part through *residuals*, which represent the measure of error with which, at each iteration, the numerical solution satisfies the governing equation discretized on the control volume. After finite volume discretization, each equation takes the form of a balance between incoming flows, outgoing flows, and source terms. The residual expresses the difference between the value obtained from this balance and the value that should be exactly satisfied in the convergent solution:

$$R_j = (\text{Incoming flows} - \text{Outgoing flows} + \text{Source terms})_j$$

where R_j is the residual associated with the j-th control volume.

However, in both non-reactive and reactive simulations, residuals alone are not sufficient to determine convergence, as they can stabilize even in the presence of motion fields or scalars that are not yet stationary. For this reason, it is necessary to combine them with physical monitors that allow the effective stabilization of the fundamental flow quantities to be verified.

In this work, the reference quantities adopted were the average temperature of the mass present in the domain and the flow rate at the nozzle outlet, monitored throughout the simulation to verify the achievement of the steady-state condition.

7.2 Non-Reactive Simulation

Non-reactive simulation is used as a preliminary transitional phase prior to the activation of chemistry. This step allows a physically stable and consistent motion field to be obtained, avoiding the immediate introduction of the strong numerical rigidity associated with reactive processes.

The presence of high flow accelerations, very thin boundary layers, and possible recirculation zones makes the domain sensitive to initial conditions. Evolving the solution first in a non-reactive regime therefore allows us to start from a more regular and stable state, improving the robustness and convergence of the subsequent reactive simulation.

The non-reactive simulation was obtained by deactivating the resolution of chemical reactions within the domain, thus keeping only the transport of species active without any production or consumption terms. In this configuration, only the equations of motion, turbulence, and ethylene transport were solved, while all other equations related to reactive processes were deactivated.

In this case, the oxygen equations remain enabled by default, as Fluent automatically includes them in the species transport model even in the absence of chemistry.

7.2.1 Initialization

Initialization is the process by which Fluent assigns an initial value to all motion field variables before starting iterations.

Its purpose is to provide the solution with a physically plausible starting point. Good initialization reduces the number of iterations required for convergence and helps avoid numerical divergences or oscillations, especially in complex domains or those characterized by strong gradients.

For this simulation, the *Standard Initialization* option was used, which allows you to manually set initial values such as pressure, velocity, and temperature within the domain, ensuring direct control over the starting state of the calculation.

In this case, the values used for initialization are shown in Table 7.1.

Gauge Pressure (Pa)	94825
Axial Velocity (m/s)	0
Radial Velocity (m/s)	0
Turbulent Kinetic Energy (m^2/s^2)	1
Specific Dissipation Rate (s^{-1})	1
O_2	1
Temperature (K)	280

Table 7.1: Initialization parameters

The values shown represent a simple and stable initial state, consistent with the operating conditions of the case. The initial pressure was set to avoid discontinuities between the inlet and outlet, while the zero velocities allow the motion field to develop naturally during the first iterations.

Furthermore, the domain is initialized entirely with O_2 because, in the non-reactive phase, there are still no combustion products and this choice ensures a uniform initial composition.

The most significant fields for characterizing motion in the non-reactive phase are shown below.

Temperature Flowfield

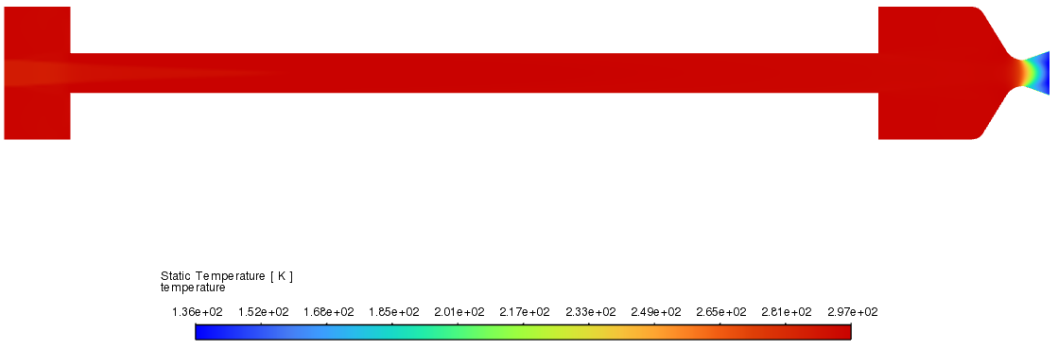

Figure 7.1: Temperature flowfield

The **temperature** range shown in Figure 7.1 is almost uniform along the port, as expected in a non-reactive case without heat sources. The slight variations present are attributable exclusively to convective and diffusive processes associated with the inlet flow, without any contribution related to chemical kinetics. The

trend obtained confirms that the thermal distribution is determined solely by the boundary conditions and the flow dynamics.

Mach Flowfield

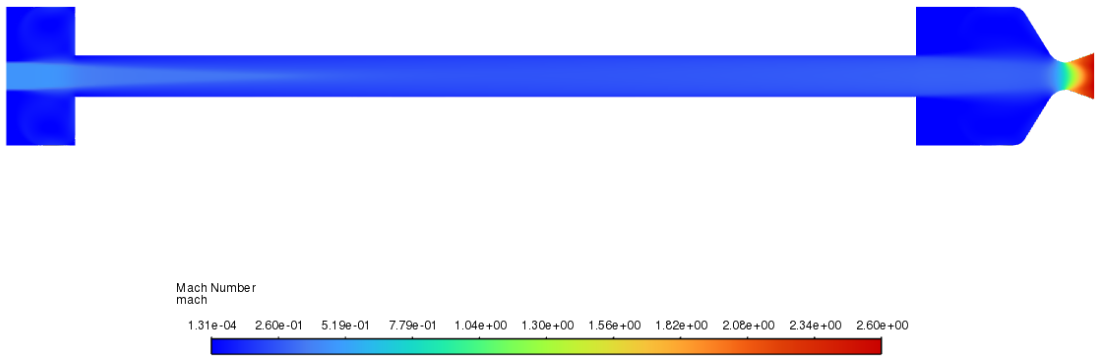

Figure 7.2: Mach flowfield

The **Mach** field shown in Figure 7.2 shows a completely subsonic flow along the port, with a progressive acceleration towards the outlet due to the pressure variation and the geometry of the duct.

O_2 Mass Fraction Flowfield

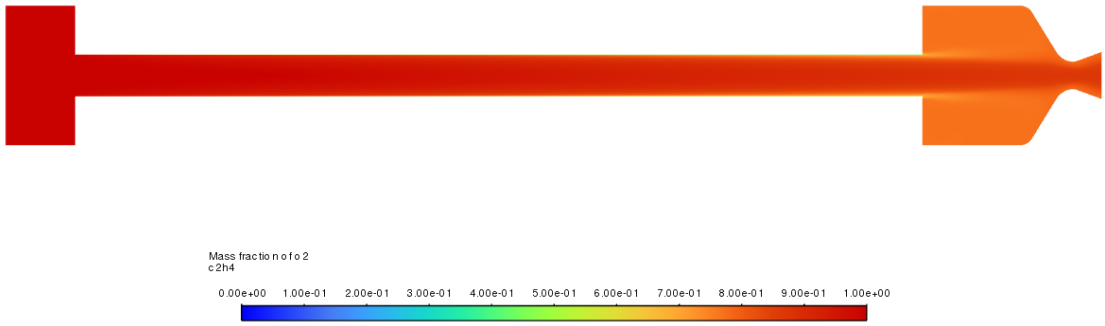

Figure 7.3: O_2 mass fraction flowfield

The distribution of the **O_2 mass fraction** shown in Figure 7.3 shows a uniform field at the inlet and a progressive variation along the port due exclusively to convective and diffusive processes. In the absence of combustion, the oxidant passes through the domain without being consumed, and its evolution reflects only the dynamics

of the flow. The absence of local accumulations or non-physical gradients confirms the numerical stability of the solution and the consistency of the non-reactive case.

The mixture is treated as binary O_2/C_2H_4, therefore the mass fraction of fuel is equal to the complement of one of that of the oxidant.

7.3 Reactive Simulation

Once convergence of the non-reactive case was achieved, chemical kinetics were activated within the domain.

The activation of chemistry involves the reactivation of the transport equations of all species involved and the introduction of source terms associated with the reactions. In this way, the model moves from a purely fluid dynamic description to a complete thermochemical configuration, in which the mixing of oxidizer and fuel generates heat release, density variations, and changes in the flow pattern.

The reference chemical mechanism is San Diego Mech (UCSD), chosen for its excellent predictive behavior under high temperature and pressure conditions.

To initiate combustion, an ignition region was defined in the initial area of the grain, in which a temperature of 2200 K was imposed. This local heating allows the reactions to be triggered and brings the system to the reactive regime, since there is no spontaneous ignition mechanism in the model adopted.

Figure 7.4 shows the position and extent of the area where the initial thermal field was applied.

Figure 7.4: Ignition region

In subsequent iterations, the flame develops and extends along the port towards the nozzle.

The initial local ignition generates a hot front that progressively activates reactions in adjacent areas, where the O_2/C_2H_4 mixture reaches temperatures sufficient for oxidation. As combustion proceeds, the increase in temperature and the reduction in density induce a slight acceleration of the flow, further favoring the propagation of the front downstream.

The system then tends to stabilize in a reactive state in which the heat release is concentrated in the regions close to the fuel wall, consistent with the typical configuration of hybrid combustion.

Once the reactive simulation converged with all active sources, the heat contribution associated with pyrolysis on the grain wall was added.

This modification made it possible to isolate the effect of heat release due to combustion in the flow, eliminating the energy input linked to the fuel regression model.

Following the modification, the simulation was brought to convergence again, monitoring the mass-weighted temperature trend, used as a global indicator of numerical stability. This quantity showed a progressive reduction until it stabilized at a lower value, confirming the new thermal equilibrium of the system with pyrolysis activated.

Temperature Range

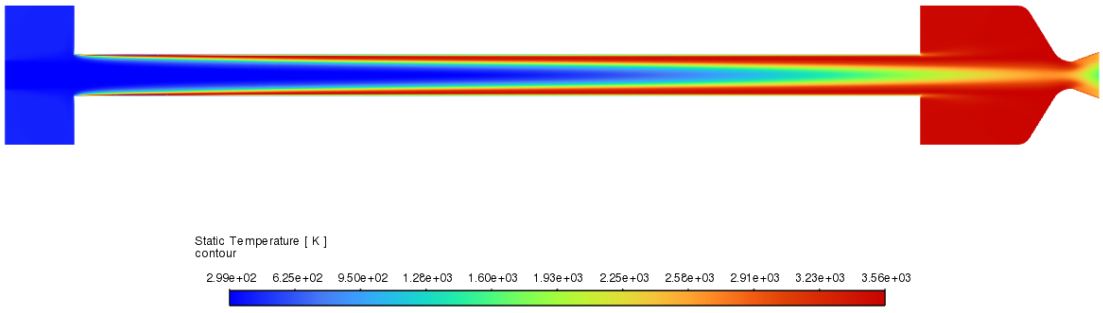

Figure 7.5: Temperature range

The **temperature** range shown in Figure 7.5 represents the thermal equilibrium reached by the system after the heat contribution associated with pyrolysis was included.

The distribution highlights a hot zone located in the region where the oxidant-fuel mixture reaches conditions favorable to oxidation, while the temperature decreases along the port due to the expansion and dilution of the products. The trend obtained is stable and consistent with the new equilibrium imposed, as confirmed by the convergence of the temperature weighted on the mass used as a numerical monitor.

Velocity Flowfield

The **velocity** flowfield shown in Figure 7.6 shows the effect of combustion on the fluid dynamics of the flow.

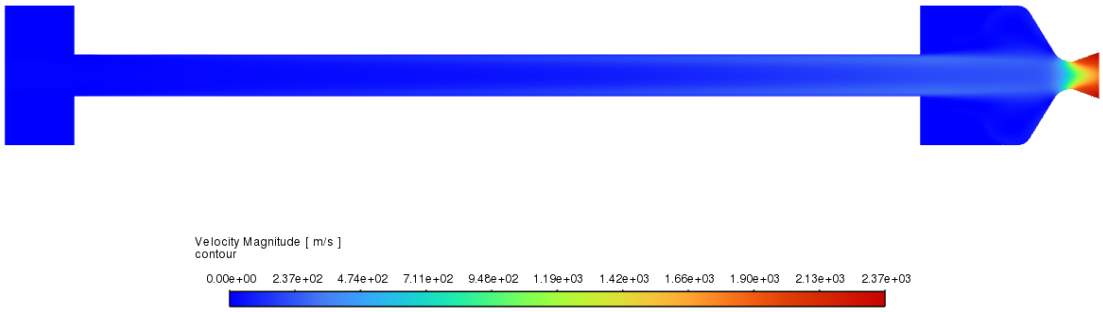

Figure 7.6: Velocity flowfield

The increase in temperature in the reacting regions leads to a local reduction in density and an acceleration of the flow along the port, with a more pronounced profile in the central area and a thickened boundary layer near the wall.

The distribution shows a progressive acceleration in the direction of the nozzle, consistent with the expansion of hot gases and the imposed pressure gradient.

Chemical Species Flowfield

The field of **O_2 mass fraction** shown in Figure 7.7 highlights the progressive consumption of the oxidant in regions where the temperature is sufficient to sustain combustion.

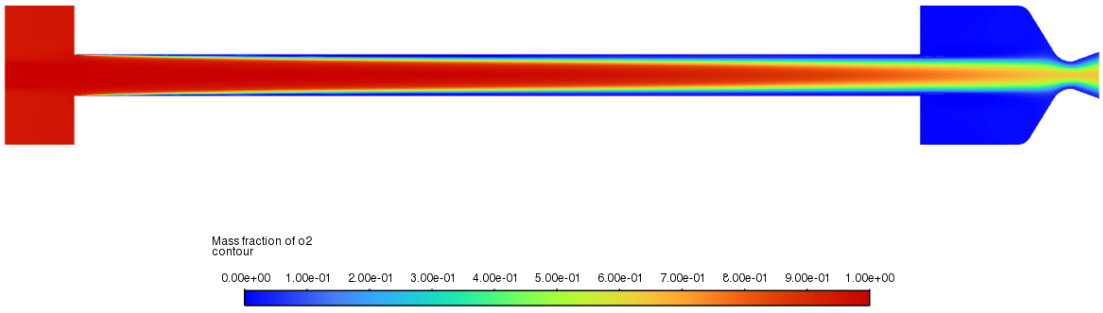

Figure 7.7: Mass fraction flowfield of the oxidant

Oxygen enters the port with a uniform distribution and is gradually reduced as the flow advances downstream, with a more marked decrease in the areas close to the wall, where mixing with the pyrolyzed fuel is more intense.

Figure 7.8 shows the field of **mass fraction of C_2H_4**, showing the distribution of the gaseous fuel inside the port during the reactant regime.

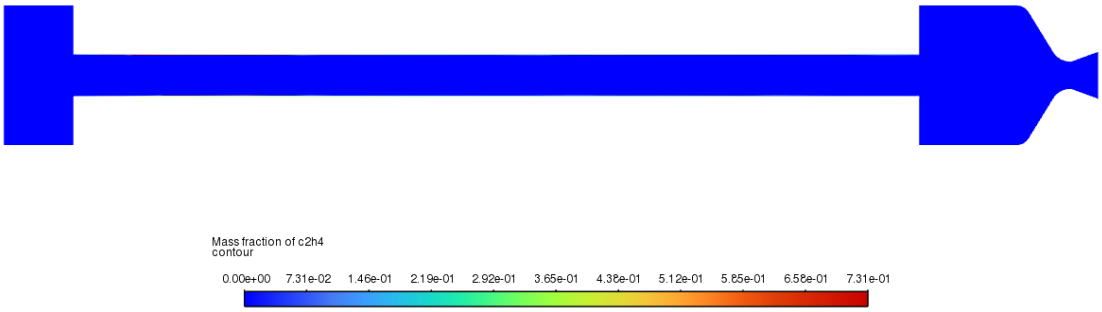

Figure 7.8: Mass fraction flowfield of the fuel

Ethylene is confined to a very thin layer adjacent to the wall, where it is released from the solid fuel and conveyed into the boundary layer before mixing with the oxidant, as shown in Figure 7.9.

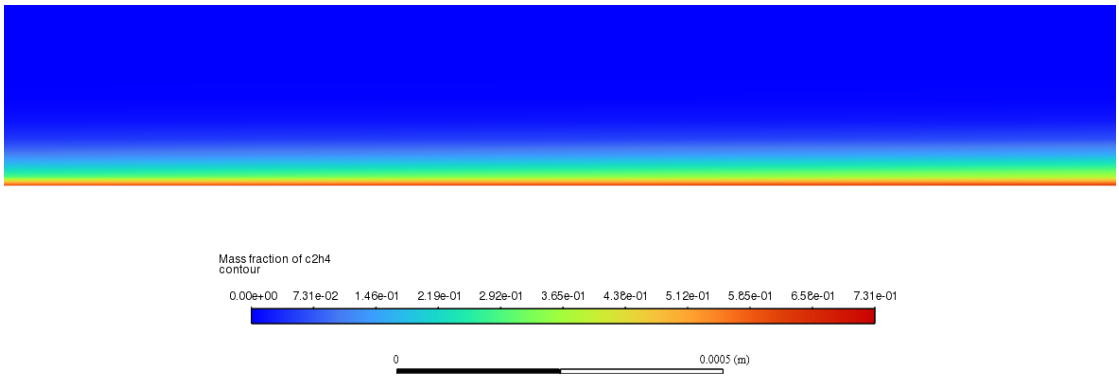

Figure 7.9: Zoom on the fuel field at the wall

Its concentration decreases rapidly along the axial direction, in areas where convective transport and temperature reach values sufficient to sustain oxidation.

Finally, Figure 7.10 shows the field of **CO_2 mass fraction**, highlighting the distribution of the main combustion product within the port.

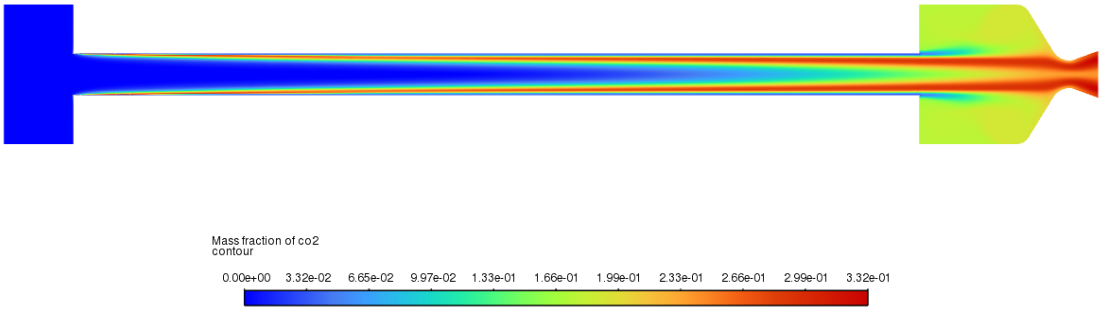

Figure 7.10: Field of CO_2 mass fraction

The concentration of carbon dioxide increases in regions where the fuel and oxidant react effectively, i.e., in areas close to the wall where the reactant boundary layer is most active. The CO_2 is then transported downstream by the hot flow, as evidenced by the development of the plume along the port.

The distribution obtained provides a direct indication of the progress of combustion, since CO_2 is formed exclusively where the reaction is thermochemically active.

Heat of Reaction Flowfield

Figure 7.11 shows the **heat of reaction** field, which represents the local distribution of the thermal release associated with the oxidation processes.

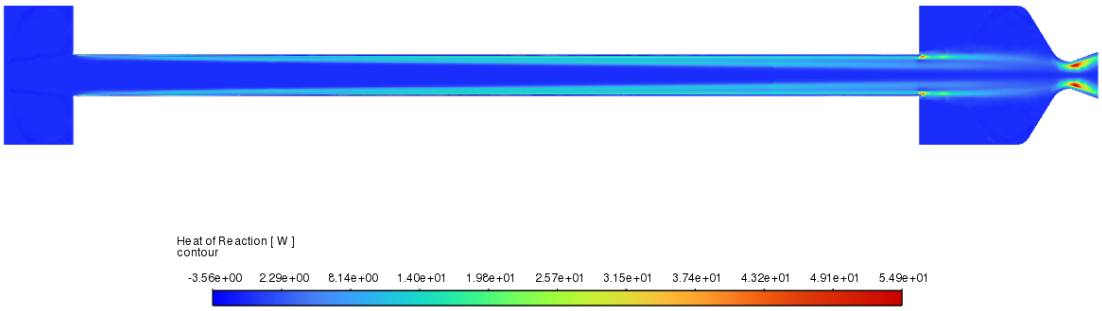

Figure 7.11: Reaction heat field

The heat release is concentrated in the wall-side reactant boundary layer, where the gaseous fuel released from the grain mixes with the oxidant and reaches conditions sufficient to sustain combustion.

The intensity of the reaction heat decreases along the axial direction, following the natural evolution of the reactant zone and the convective transport of the hot flow.

The distribution of reaction heat highlights the region where combustion is active. This is consistent with the consumption of O_2, the presence of a thin layer of C_2H_4 at the wall, and the formation of CO_2.

This field is therefore a direct indicator of the flame structure and the thermo-chemical balance of the system.

At the nozzle throat, there is a significant peak in the source term in the energy equation associated with chemical reactions. In this region, mass fraction analysis shows an increase in OH radicals and O atoms, while the concentration of H is negligible. At the same time, the static temperature does not show a further increase compared to the combustion chamber, suggesting that the energy generated by the direct reactions is balanced, and partly compensated, by the endothermic contribution of the reverse dissociation reactions. This behavior is consistent with the presence of high-temperature dissociation processes, favored by the thermo-fluid dynamic conditions typical of the throat (high acceleration and pressure reduction), rather than with the ignition of additional combustion.

Figures 7.12a and 7.12b below show two comparative graphs illustrating the distribution of the species just discussed: the first includes all significant species, while the second shows the subset of radicals and atoms, excluding the main stable and molecular products, in order to highlight their local increase in the throat.

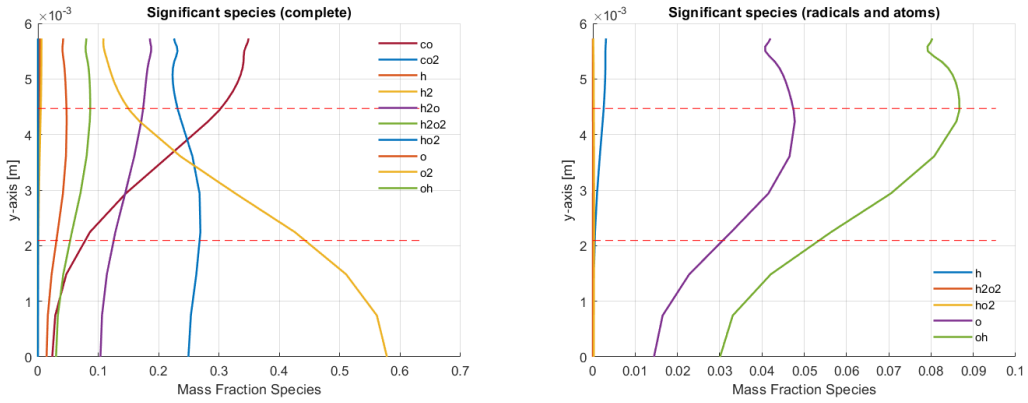

(a) Main chemical species **(b)** Radicals and atomic species

Figure 7.12: Species present at the peak of reaction heat in the throat

The throat is therefore configured as an area where the mixture tends towards a partially dissociated chemical equilibrium state, rather than as an additional combustion region.

Chapter 8

Model Validation

CFD simulations provide an approximate solution to the equations describing fluid motion. This approximation inevitably introduces uncertainties due to various factors, including the chemical model, physical modeling, numerical discretization, and boundary conditions.

Consequently, each CFD result must be interpreted considering the margin of uncertainty associated with the assumptions and simplifications used and must be validated through comparisons with experimental data or sensitivity analyses.

8.1 Chemical Uncertainty

In reactant simulations, a significant part of the uncertainty stems from chemical modeling. Chemical mechanisms are constructed from thousands of experimental measurements and theoretical estimates, often obtained under conditions very different from those in the combustion chamber.

Furthermore, the need to use reduced mechanisms or simplified couplings (e.g., EDC, finite-rate without TCI) introduces additional approximations.

For this reason, chemical uncertainty is one of the main contributors to the margin of error in reactive simulations and must be considered when evaluating results.

To evaluate the impact of chemical uncertainty, simulations were performed with different mechanisms, as described in chapter 5.5. These include the San Diego Mechanism (UCSD), whose results are reported in chapter 7.3, Lu's reduced mechanism, and Chang's skeletal mechanism.

The comparison was conducted using the characteristic velocity c^*, the chamber pressure p_c, and the outlet mass flow rate $\dot{m}$, for which known experimental data are available for the case analyzed, as reported in Tables 4.1 and 4.2.

The main flow fields used for the comparison between the different chemical

mechanisms are presented below.

Temperature fields

Figure 8.1 shows the temperature contours obtained with the three chemical mechanisms considered. In all simulations, the thermal profile at the flame zone is comparable, with a peak of approximately 3500 K, a value consistent with the estimates provided by the CEA shown in table 4.3.

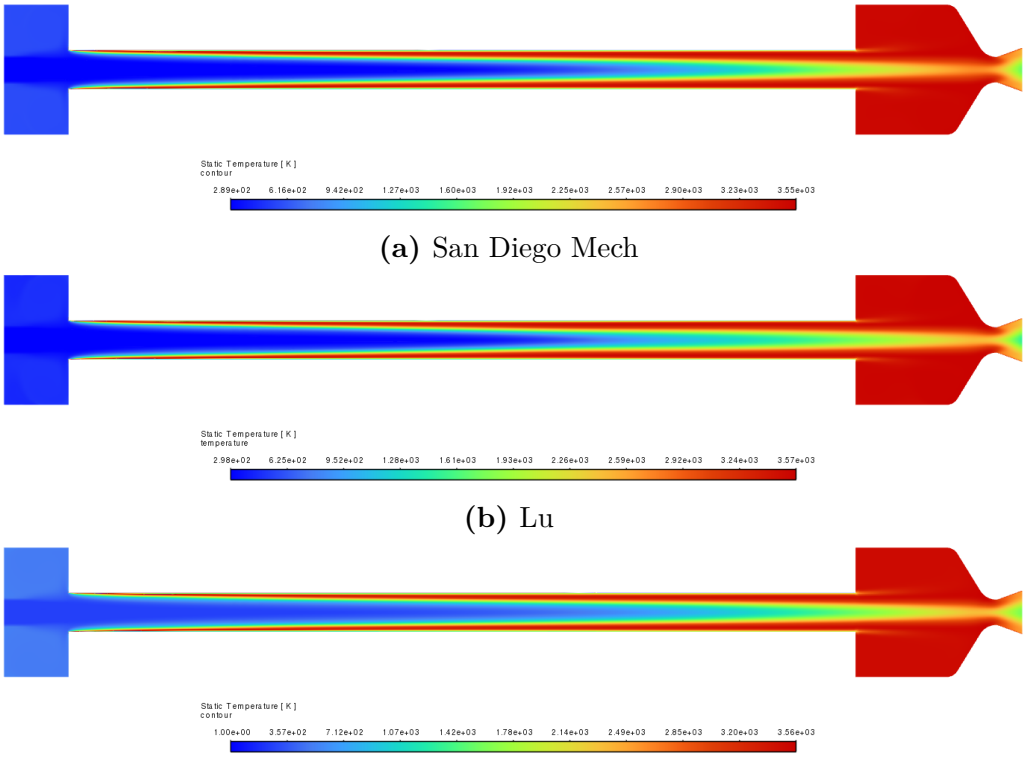

(a) San Diego Mech

(b) Lu

(c) Chang

Figure 8.1: Comparison of temperature fields

As shown in Table 8.1, the three kinetic mechanisms predict very similar peak temperatures, with differences of only a few tens of Kelvin.

	San Diego Mech	Lu	Chang
T_{max} (K)	3550	3570	3560

Table 8.1: Temperatures in different chemical mechanisms

Pressure fields

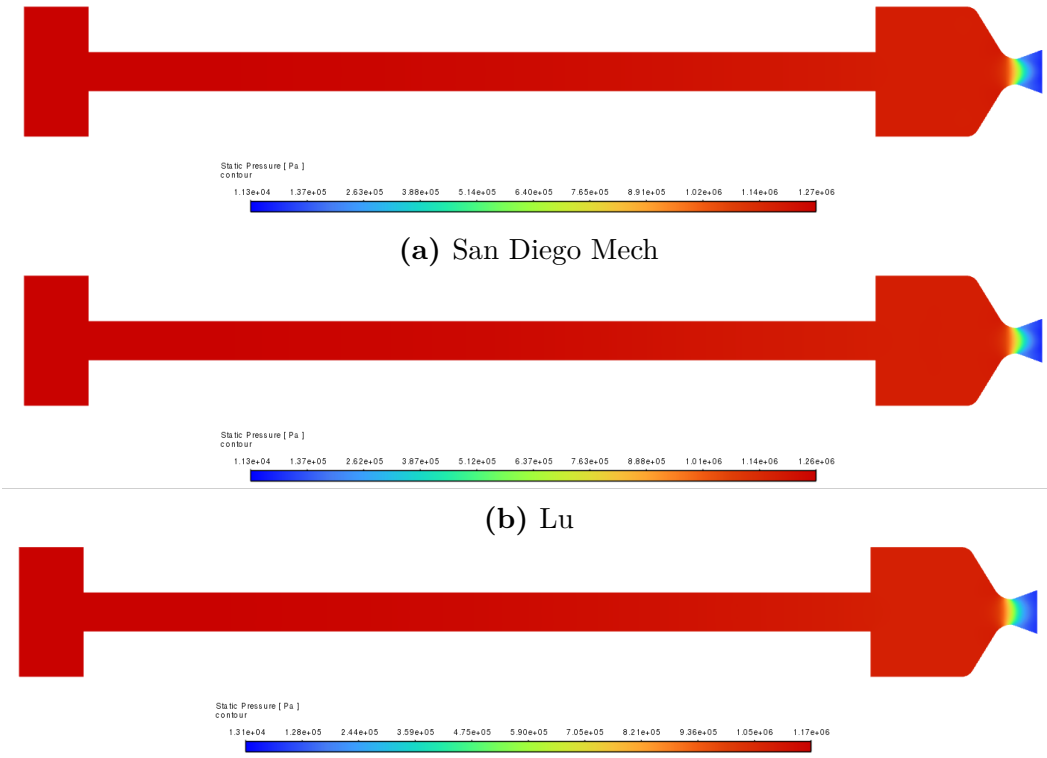

(a) San Diego Mech

(b) Lu

(c) Chang

Figure 8.2: Comparison of pressure fields

The pressure distribution in the three models is comparable. The chamber maintains values consistent with the experimental ones, and the differences between chemical mechanisms are subtle, indicating that the pressure is not very sensitive to the variations introduced by the chemistry itself.

The pressure values estimated using the different chemical mechanisms are shown in Table 8.2. These values were calculated by integrating over the volume of the chamber, using a mass-weighted average of the pressure field.

	San Diego Mech	Lu	Chang	Experimental data (Karbeyoglu)
p_c (atm)	12.48	12.41	11.51	12.5
$Err_{\%}$ (%)	0.16	0.72	8	-

Table 8.2: Pressures in the different chemical mechanisms

Reaction heat field

Figure 8.3 shows the reaction heat contours for the three chemical mechanisms considered. The spatial distribution of the maximum heat release zone is similar overall, with a reaction front located near the fuel wall and an increase in heat release towards the throat. However, there are noticeable differences in the intensity of the peak: the San Diego Mechanism and the reduced Lu model tend to predict a more intense and slightly more concentrated reaction heat band, while the Chang model shows a more rounded profile.

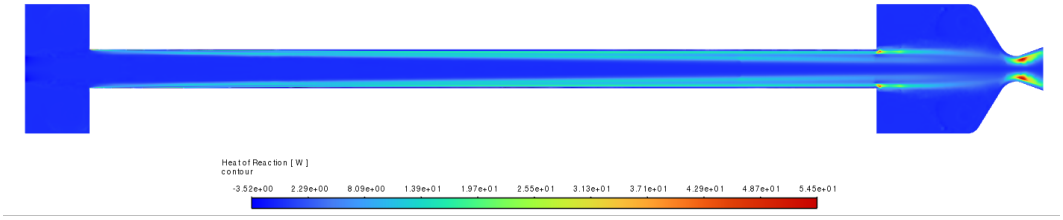

(a) San Diego Mech

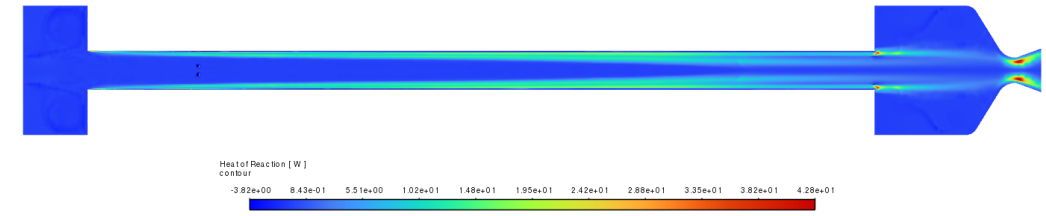

(b) Lu

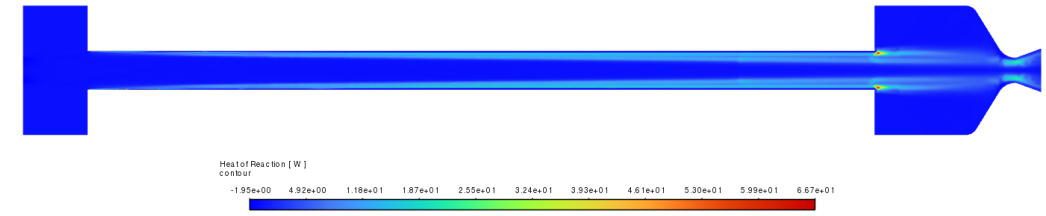

(c) Chang

Figure 8.3: Comparison of reaction heat fields

Although these discrepancies do not drastically alter the overall structure of the flame, they have a direct impact on integrated quantities such as average temperature, chamber pressure, and overall engine performance.

The comparison of reaction heats therefore confirms that the choice of kinetic mechanism affects not only the species but also the distribution of energy release, contributing significantly to the overall uncertainty of the reactive simulations.

Comparison of c^*

For a general comparison between the various models, it was decided to use the characteristic velocity c^*.

The parameter was calculated using equation 1.1, employing the throat area obtained from table 4.2, the pressures obtained from the simulations and reported in Table 8.2, and the mass flow rates determined by a surface integral at the domain exit. These are reported in the following table:

	San Diego Mech	Lu	Chang
$\dot{m}$ (kg/s)	0.0557270	0.0577255	0.0557346

Table 8.3: Comparison of flow rates $\dot{m}$

Table 8.4 shows the calculated values and their respective relative errors.

	San Diego Mech	Lu	Chang	Experimental data (Karbeyoglu)
c^* (m/s)	1682	1672	1552	1705
$Err_{\%}$ (%)	1.35	1.93	9	-

Table 8.4: Comparison c^*

8.2 Boundary layer

One of the most immediate checks on the reliability of the simulation concerns the consistency of the boundary layer that develops along the fuel wall. The structure of the boundary layer is determined exclusively by the flow dynamics and the thermophysical properties of the fluid; for this reason, it is a particularly sensitive indicator of numerical accuracy and mesh quality.

Validation through the boundary layer consists of verifying that the hydrodynamic and thermal thicknesses evolve with a trend compatible with the available theory for compressible flows in laminar or turbulent regimes, depending on local conditions.

8.2.1 Kinematic boundary layer

To quantify the thickness of the hydrodynamic boundary layer, the classic reference criterion was used, defining δ_{99} as the distance from the wall at which the local

velocity reaches 99% of the velocity outside the boundary layer. The extraction was performed along several axial sections in the domain, interpolating the velocity profiles predicted by Fluent and identifying the point where the condition occurs:

$$u(y = \delta_{99}) = 0.99\, u_\infty$$

The use of multiple sections along the domain allowed us to analyze the growth of the boundary layer and verify that the increase in $\delta_{99}(x)$ is physically plausible.

Figure 8.4 shows the trend of the boundary layer thickness along the duct, obtained by interpolating the velocity profiles extracted in different sections.

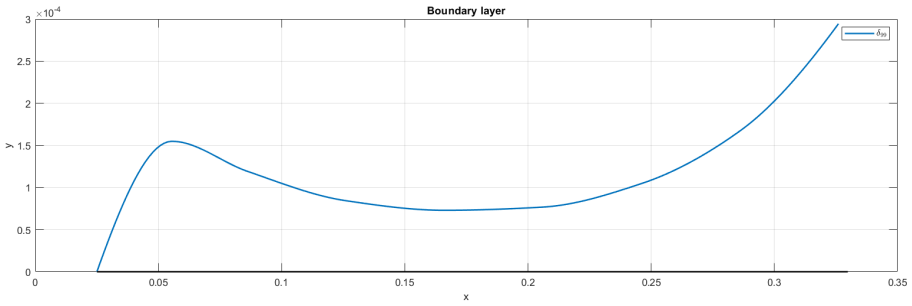

Figure 8.4: Trend of boundary layer thickness along the port.

From the distribution of the velocity profiles, it can be seen that the boundary layer is particularly thin, since the increase in velocity near the wall occurs over a very small thickness. This behavior is shown in Figure 8.5.

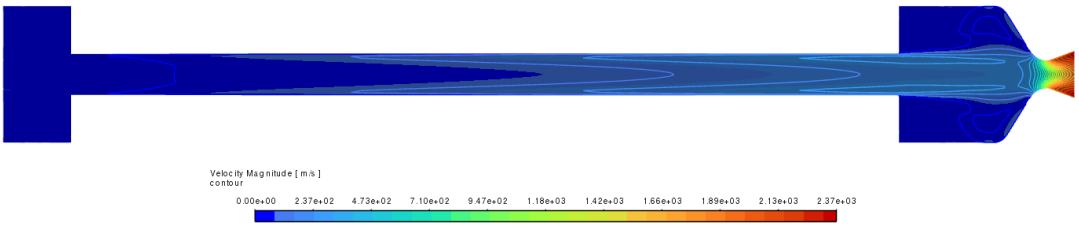

Figure 8.5: Velocity profiles near the wall.

The trend obtained is in agreement with that reported in Chapter 7 of *Fundamentals of Hybrid Rocket Combustion and Propulsion* [2], which shows velocity profiles with similar characteristics (Figure 8.6).

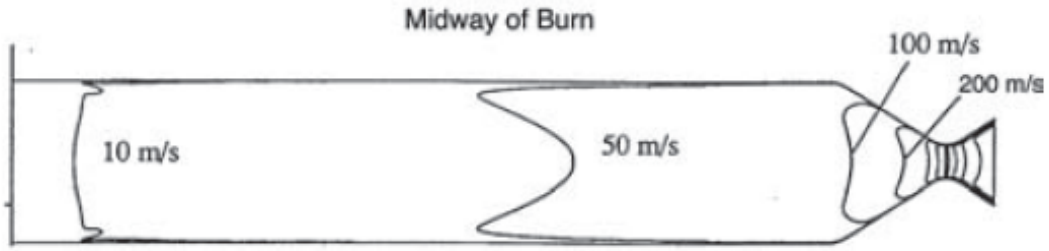

Figure 8.6: Typical velocity profiles reported in [2].

This behavior is attributable to the strong acceleration of the gases near the wall, due to both the addition of heat and the increase in mass flow rate. As we move away from the wall, the influence of these effects is reduced and the acceleration of the gases gradually decreases [2].

The steep slope of the velocity profile near the wall shows that the gases accelerate rapidly within the boundary layer.

From a physical point of view, the strong acceleration of the fluid tends to compress the velocity profile toward the wall, limiting the region in which viscosity is able to diffuse momentum. Under these conditions, viscous diffusion cannot compensate for the acceleration imposed by the flow, and the thickness δ_{99} remains very small throughout the duct.

8.3 Grid convergence analysis

Grid convergence analysis is a fundamental tool for evaluating the reliability of CFD simulations. The numerical solution of a flow problem depends on the spatial discretization chosen: changing the size of the cells changes the accuracy with which gradients, convective and diffusive flows, and, in general, the terms of the governing equations are approximated. Without a sensitivity check with respect to the mesh, it is not possible to determine whether the results obtained are truly representative of the physical behavior or whether they depend on the particular discretization adopted.

The objective of grid convergence analysis is to measure how a quantity of interest (e.g., chamber pressure, characteristic velocity, flame temperature, mass flow rate) varies when moving from a coarse grid to a progressively finer one. If this variation tends to decrease until it becomes negligible, the solution is said to be "grid-independent ." In this way, it is possible to identify a level of discretization that guarantees a good compromise between computational cost and accuracy.

To quantify the numerical error and estimate the asymptotic value towards which the solution converges, Richardson extrapolation is often used. This tool

allows us to evaluate not only the convergence trend, but also the effective order of the numerical scheme and the margin of uncertainty associated with discretization.

8.3.1 Evaluation of the grid convergence order

To evaluate the effect of discretization on the quality of the solution, the convergence order p was analyzed, i.e., the measure of how quickly the numerical error decreases when the mesh is refined. The error introduced by the mesh can be written as:

$$h_1 \rightarrow E_1 = k\, h_1^p \tag{8.1}$$

where k is a constant that depends on the physical problem considered, the formulation of the governing equations, and the specific numerical scheme used (e.g., order of interpolation, treatment of gradients and convective flows).

By performing multiple simulations with different characteristic lengths h_1 and h_2, it is possible to estimate the order of convergence as:

$$p = \frac{\ln\left(\frac{E_1}{E_2}\right)}{\ln\left(\frac{h_1}{h_2}\right)}$$

This value allows us to verify whether the behavior of the solution complies with the theoretical order predicted by the numerical schemes adopted and whether the chosen discretization is sufficiently fine to reduce the truncation error.

In other words, it describes the efficiency of the numerical scheme: a higher order indicates that the error decreases more rapidly as the characteristic size of the cell decreases.

Simulations were therefore carried out using different characteristic lengths of the mesh, comparing the trend of the quantities of interest as the discretization varied.

The output flow rate was chosen as the evaluation parameter, as it is a direct indicator of the correctness of the mass balance and the physical consistency of the entire domain.

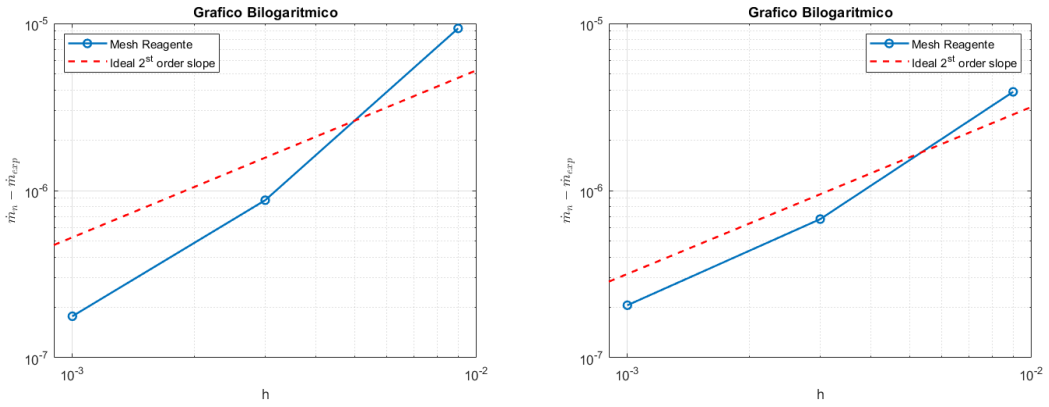

(a) Non-Reagent **(b)** Reactive

Figure 8.7: Bilogarithmic graph

In order to analyze the accuracy of the spatial discretization scheme, bilogarithmic graphs of the error were plotted as the characteristic grid length h varied, for both the non-reactive and reactive cases (Figure 8.7a and Figure 8.7b).

In both simulations, it can be seen that, as h decreases, the curves progressively tend to assume a slope close to the theoretical value $p_{\text{th}} = 2$, consistent with the use of the *Second Order Upwind* scheme.

For coarser grids, on the other hand, the deviation from the expected slope is more evident, indicating that the solution has not yet reached the asymptotic convergence regime and that the numerical error is not entirely dominated by the second-order term.

The realignment of the slopes with the refinement of the mesh, present in both the non-reactive and reactive flows, despite the addition of chemical source terms, confirms that the order of accuracy of the scheme is correctly achieved from a numerical point of view and that the discretization error becomes asymptotically consistent with the expected second order.

Tables 8.5 and 8.6, shown below, collect the total mass flow rate values $\dot{m}$, the discretization errors E_i, and the empirical convergence orders p used for plotting the bilogarithmic graphs.

h (m)	0.001	0.003	0.009
$\dot{m}$ (kg/s)	0.05572708	0.055728133	0.055717914
E_i	1.770E-07	8.760E-07	9.343E-06
p	1.45	2.15	-

Table 8.5: Non-Reactive

h (m)	0.001	0.003	0.009
$\dot{m}$ (kg/s)	0.055727051	0.055726582	0.055723359
E_i	2.060E-07	6.750E-07	3.898E-06
p	1.08	1.6	-

Table 8.6: Reagent

Tables 8.5 and 8.6 show that the error E_i increases as h increases in both cases, as expected when using increasingly less accurate discretization.

In the non-reactive case, the regular increase in E_i as we move towards coarser grids suggests a behavior that is qualitatively compatible with the asymptotic regime of discretization.

In the reactive case, the growth of the error is less regular. This is probably due to the strong coupling between flow and chemistry, which introduces a more pronounced nonlinearity than in the non-reactive case. This additional complexity makes it more difficult to achieve a fully asymptotic trend and makes the error more sensitive to small local variations in the mesh and residual iterative inaccuracies.

8.3.2 Richardson Extrapolation with Theoretical Order

Richardson extrapolation is a classic tool for evaluating numerical accuracy and estimating the "true" value of a quantity calculated using discrete methods.

Knowing the theoretical order of the numerical scheme used, it is possible to combine the results obtained with meshes of different fineness to eliminate, or at least reduce, the dominant term of the discretization error.

Starting from equation 8.1, it is possible to calculate an estimate of the exact solution as:

$$u_0 \approx \frac{r^p\, u_h - u_{rh}}{r^p - 1}$$

where r is the factor by which the characteristic length h is modified, in this case $r = 3$, while $p = p_{\text{th}} = 2$ for the *Second Order Upwind* numerical scheme.

The two most accurate simulations are considered:

	Non-Reactive	Reactive
E_{abs}	3.086E-07	1.474E-07
E_{rel} (%)	0.001	0.0003

Table 8.7: Errors in flow rate calculated with theoretical order

The absolute errors with respect to the reference are very small in both cases, with values less than 10^{-5}, and decrease further in the reactive case.

8.3.3 Richardson Extrapolation with Empirical Order

To estimate the value closest to the "exact" solution from the discrete results, Richardson extrapolation can be applied using the empirical convergence order p_{emp}. This is obtained from the equation:

$$p = \frac{\ln\left(\frac{u_3 - u_2}{u_2 - u_1}\right)}{\ln(r)}$$

Denoting by u_h and u_{rh} the solutions obtained with the finest and coarsest meshes, respectively, and assuming that the dominant discretization error follows the form $E \propto h^p$, the estimate of the exact solution u_0 is obtained by:

$$u_0 = u_h - \frac{u_{rh} - u_h}{r^p - 1}$$

The values obtained are shown in table 8.8

	Non-Reactive	Reactive
p_{emp}	2	1.75
E_{abs}	2.980E-07	1.2613E-07
E_{rel} (%)	0.0005	0.0002

Table 8.8: Errors in flow rate calculated with empirical order

In this work, the grid refinement analysis returned an empirical convergence order $p_{emp} = 2$ for the non-reactive case and $p_{emp} = 1.75$ for the reactive case, values that are indicative of a discretization that approaches the asymptotic regime.

The adoption of p_{emp} allowed for a more accurate characterization of the dominant discretization error, resulting in a decrease in estimated errors compared to the evaluation based on the theoretical order.

8.4 Conclusions

The objective of this work was to model a hybrid rocket engine using CFD simulations developed with ANSYS Fluent.

In particular, the geometry of a GOX/HDPE hybrid engine was implemented, the physical and chemical models required to describe the combustion process were defined, and the main thermo-fluid dynamic quantities within the chamber and the nozzle throat were analyzed.

A preliminary validation of the chemistry was also conducted by comparing different mechanisms available in the literature, verifying the consistency of the thermal fields and the main species.

At the same time, numerical uncertainties were evaluated through a grid convergence study in order to analyze the stability of the solution and the sensitivity of the flow rates and key variables to spatial refinement.

The analysis of the results reveals the following main considerations:

- The comparison between the temperature fields obtained with three different chemical mechanisms shows qualitative consistency in the bulk of the flow, indicating that the models reproduce globally comparable thermal trends, with limited local deviations that are not dominant for the purposes of macroscopic analysis.

- The peak in the heat of reaction observed in the throat is not attributable to additional combustion, but to a region dominated by dissociation reactions. This behavior is confirmed by the local increase in OH radicals and O atoms in the absence of a corresponding increase in static temperature.

- The *characteristic velocity* c^* predicted by the simulations shows good agreement with the experimental reference value, with a minimum error of 1.35% and a maximum deviation of about 9%, depending on the chemical mechanism considered.

- The *bilogarithmic graphs* of the error show that, as the characteristic length of the grid h decreases, the slope of the curves approaches the theoretical value $p_{th} = 2$ of the Second Order Upwind scheme, both in the non-reactive and reactive cases. This indicates that the solution enters the asymptotic regime dominated by the second-order discretization term.

- The grid convergence analysis shows a progressive reduction of the error as the mesh is refined. After applying Richardson extrapolation, the mass-flow errors decrease further, reaching values as low as 0.0002%. This result confirms the absence of spurious numerical effects and indicates that the remaining error is mainly due to grid discretization.

Limitations of the Work

- The empirical estimate of the order of convergence is not very robust when the differences between solutions on successive meshes become very small, as the logarithmic formula amplifies numerical noise.
- The absence of experimental data on dissociated species in the throat prevents a complete quantitative validation of the local chemistry.

The developed model also provides a solid basis for future parametric analyses , allowing the influence of the oxidizing flow rate, the O/F ratio, and the port geometry on engine performance and the thermo-fluid dynamic behavior of the system to be evaluated.

Future Developments

Possible extensions of the work include:

- Extension of the model to include **radiation**, to quantify its contribution in high-temperature regions and evaluate its impact on the overall energy balance.
- Development of a **fully coupled** model, in which flow, chemical kinetics, radiation, and conduction in the wall are solved simultaneously, with the aim of describing the thermo-structural interactions of the system in an integrated manner.
- Analysis with more extensive chemical mechanisms including **intermediate hydrocarbon species**, to evaluate the influence of kinetic detail in the expansion region and the sensitivity of the thermal field to chemical modeling.
- Introduction of **dynamic fuel regression**, using dynamic mesh and a coupled ablation/pyrolysis model, to simulate the actual evolution of the port area and its effect on flow variables.

In conclusion, the work provides a consistent numerical description of the energy peak in the throat, confirms convergence behavior compatible with second-order discretization, and demonstrates the overall consistency of the calculated quantities.

However, there is still room for further refinement, especially with regard to the modeling of pyrolysis, the radiative contribution, fuel regression, and comparison with local experimental data, aspects that can be explored in future developments.

Bibliography

[1] *Types of chemical rocket engines*. 2011. URL: https://www.sciencelearn.org.nz/resources/393-types-of-chemical-rocket-engines (cit. on pp. 3, 4).

[2] Kenneth K. Kuo and Martin J. Chiaverini. *Fundamentals of Hybrid Rocket Combustion and Propulsion*. AIAA, 2007 (cit. on pp. 8, 10, 15, 22, 23, 77, 78).

[3] Ronald Humble. *Space Propulsion Analysis and Design*. McGraw-Hill Higher Education, 1995 (cit. on p. 12).

[4] Elizabeth Therese Jens Ashley Chandler Karp. *Hybrid Rocket Propulsion Design Handbook*. Academic Press, 2023 (cit. on p. 17).

[5] C. Glaser, J. Hijlkema, and Anthoine J. «Evaluation of Regression Rate Enhancing Concepts and Techniques for Hybrid Rocket Engines». In: *Aerotecnica Missili & Spazio* (2022) (cit. on p. 18).

[6] D. Bianchi, G. Leccese, F. Nasuti, M. Onofri, and C. Carmicino. «Modeling of High Density Polyethylene Regression Rate in the Simulation of Hybrid Rocket Flowfields». In: *MDPI* (2019) (cit. on pp. 21, 30).

[7] Arif Karabeyoglu M., Cantwell Brian J., and Stevens J. «Evaluation of the Homologous Series of Normal Alkanes as Hybrid Rocket Fuels». In: 2005 (cit. on pp. 23, 24).

[8] Sanford Gordon and Bonnie J. Mcbride. «Computer program for calculation of complex chemical equilibrium compositions and applications.» In: *NASA Reference Publication 1311* (1994). URL: https://cearun.grc.nasa.gov/ (cit. on p. 26).

[9] D. Pastrone. «Fondamenti di Endoreattori - Effetti Reali & Heat Transfer Analysis». I - Effetti in camera di combustione. 2018/19 (cit. on p. 27).

[10] Filippo Masseni. «Endoreattori - Esercitazione N.3 - Dimensionamento» (cit. on p. 27).

[11] Gontijo Maurício S., Filho Renato d., and Domingos Caio H. «Design of Pre-Combustion Chambers for Hybrid Propellant Rocket Motors and Related Aspects». In: *AIAA SciTech Forum 2023* (2023) (cit. on p. 28).

[12] Di Martino Giuseppe Daniele. «Experiments and Simulations of Hybrid Rocket Internal Flows and Material Behaviour». PhD thesis. Università degli studi di Napoli Federico II (cit. on p. 29).

[13] Ansys Inc. *ANSYS FLUENT 12.0 User's Guide*. Ansys Inc. 2009. URL: `https://www.afs.enea.it/project/neptunius/docs/fluent/html/ug/main_pre.htm` (cit. on pp. 39, 46, 47, 49, 53, 54, 59).

[14] University of California at San Diego (http://combustion.ucsd.edu). *Chemical-Kinetic Mechanisms for Combustion Applications*. 2016. URL: `http://web.eng.ucsd.edu/mae/groups/combustion/mechanism.html` (cit. on p. 51).

[15] Xu Chaoqi and Konnov Alexander A. «Validation and analysis of detailed kinetic models for ethylene combustion». In: *ELSEVIER* (2011) (cit. on p. 51).

[16] Luo Zhaoyu, Sang Yoo Chun, Richardson Edward S., Chen Jacqueline, Law Chung K., and Lu Tianfeng. «Chemical explosive mode analysis for a turbulent lifted ethylene jet flame in highly-heated coflow». In: (2012) (cit. on p. 51).

[17] Luca Stefano, Al-Khateeb Ashraf N., Attili Antonio, and Bisetti Fabrizio. «Comprehensive Validation of Skeletal Mechanism for Turbulent Premixed Methane–Air Flame Simulations». In: *Combustion and Flame* (2012) (cit. on p. 51).

[18] Yachao Chang, Ming Jia, Yaodong Liu, Yaopeng Li, and Maozhao dXie. «Development of a new skeletal mechanism for n-decane oxidation under engine-relevant conditions based on a decoupling methodology». In: (2013) (cit. on p. 52).